Inaugural dissertation
for
obtaining the doctoral degree
of the
Combined Faculty of Mathematics, Engineering and Natural Sciences
of the
Ruprecht - Karls - University
Heidelberg

Presented by

Jessica Hunger, M.Sc.

born in: Mannheim, Germany

Oral Examination: 19.06.2023

Non-invasive tracking of T cell recruitment to the tumor microenvironment in a murine glioma model by high field cellular magnetic resonance imaging

Referees: Prof. Dr. Michael Platten

Dr. Wilhelm Palm

Statutory Declaration/Eidesstattliche Versicherung

Eidesstattliche Versicherung gemäß § 8 der Promotionsordnung der Gesamtfakultät für Mathematik, Ingenieur- und Naturwissenschaften der Universität Heidelberg

1. Bei der eingereichten Dissertation mit dem Titel

....

....
handelt es sich um meine eigenständig erbrachte Leistung.

2. Ich habe nur die angegebenen Quellen und Hilfsmittel benutzt und mich keiner unzulässigen Hilfe Dritter bedient. Insbesondere habe ich wörtlich oder sinngemäß aus anderen Werken übernommene Inhalte als solche kenntlich gemacht.

3. Die Arbeit oder Teile davon habe ich bislang nicht an einer Hochschule des In- oder Auslands als Bestandteil einer Prüfungs- oder Qualifikationsleistung vorgelegt.

4. Die Richtigkeit der vorstehenden Erklärungen bestätige ich.

5. Die Bedeutung der eidesstattlichen Versicherung und die strafrechtlichen Folgen einer unrichtigen oder unvollständigen eidesstattlichen Versicherung sind mir bekannt.

Ich versichere an Eides statt, dass ich nach bestem Wissen die reine Wahrheit erklärt und nichts verschwiegen habe.

....
Ort und Datum Unterschrift

Acknowledgements

I would like to thank Michael Breckwoldt for his constant amazing supervision and for how much he cares about his students. Furthermore, I would like to thank Michael Platten for the opportunity to perform research in his lab. Thank you to the immuno-imaging team for advice and technical assistance, especially to Katharina Schregel for assisting the MRI data analysis, to Manuel Fischer for supporting the MRI acquisition and to Volker Sturm for providing the matlab script. Thank you to the whole CCU Neuroimmunology and Brain Tumor Immunology for amazing 3.5 years, especially to Dennis Alexander Agardy for his support regarding surgeries. I have very much appreciated the DKFZ community and infrastructure. Thank you to my TAC members Christiane Opitz and Wilhelm Palm for their advice and also to the UNITE community. Furthermore, I would like to thank Rachel Mellwig from EMBL for her help regarding electron microscopy and the Institute of Earth Sciences for analyzing the iron content of my cells.

Thank you to Alexander Kourtesakis and to Michael Kilian for our collaborative work on CAR T cell labeling and thank you to Alice de Roia and Walter Mier for our joint research on SSTR2 expressing T cells. Thank you to Berin Boztepe for supporting the clearing and light sheet imaging.

I would like to thank my family for their support throughout my studies and my parents for their early recognition and support of my interest in science.

Thank you, Judith, for always believing in me and for always being there.

Publications related to this thesis

Publications not related to this thesis

"T cell-independent eradication of experimental glioma by intravenous TLR7/8-agonist-loaded nanoparticles", Verena Turco, Kira Pfleiderer, Jessica Hunger, […], Michael Platten, ***Nature communications*****, 2023**

Table of contents

List of tables

List of figures

Abstract

Gliomas are characterized by increased T cell exhaustion and poor T cell infiltration into the tumor as well as an overall highly immunosuppressive tumor microenvironment (TME). Response rates in preclinical glioma models and patients to promising new therapeutic approaches in the field of immunotherapies remain heterogenous. These include checkpoint blockade, peptide and mRNA vaccines and adoptive therapy with chimeric antigen receptor (CAR) or T cell receptor (TCR)-transgenic T cells. This demonstrates the need for non-invasive tracking of T cell recruitment to the TME in order to monitor immunotherapies, adapt therapeutic strategies and predict treatment outcome. Iron oxide nanoparticles (NP) can be visualized non-invasively by magnetic resonance imaging (MRI) and dedicated MRI sequences such as T2* mapping. Using isolated murine T cell cultures I show that labeling of T cells with iron oxide NPs as contrast agents is feasible and does not impair T cell viability and functionality as assessed by cytokine secretion and antigen-specific killing activity *in vitro*. I demonstrate that adoptively transferred T cells can be visualized intratumorally in a murine glioma model by high field MRI at 9.4 Tesla with high sensitivity and that T cells can be tracked non-invasively in a time course of at least two weeks. Correlative methods include immunohistochemistry, flow cytometry, tissue clearing and light sheet microscopy. Tumor relaxation times at an early time point after adoptive cell transfer (ACT) were a predictor for tumor response or resistance, which demonstrates that non-invasive quantification of spatial and temporal T cell dynamics in the TME can facilitate immune cell monitoring to assess immunotherapy efficacy.

Zusammenfassung

Gliome sind maligne Hirntumore, die sich durch eine geringe T Zell Infiltration sowie eine hohe Expression von sogenannten T-Zell-Erschöpfungsmarkern auszeichen. Die Tumore weisen ein insgesamt immunsuppressives Tumormikromilieu auf. Das Ansprechen auf Immuntherapien wie Immuncheckpointblockade, Vakzinierungen sowie die Behandlung mit Rezeptor-transgenen T-Zellen oder CAR T-Zellen ist sowohl in der präklinischen Forschung an Mäusen als auch in klinischen Studien heterogen. Nicht-invasive Methoden zur Visualisierung der T-Zell Rekrutierung und intratumoraler T-Zell-Verteilung werden daher dringend benötigt, um das Therapieansprechen zu einem frühen Zeitpunkt vorhersagen und die Therapie dementsprechend anpassen zu können. Eisenoxidnanopartikel können nicht-invasiv mittels Magnetresonanztomographie (MRT) unter anderem durch T2* Mapping-Verfahren dargestellt werden. Ich zeige in dieser Promotionsarbeit, dass T-Zellen mit Eisenoxidnanopartikeln *in vitro* beladen werden können, ohne deren Viabilität oder Funktionalität zu beeinflussen. Adoptiv transferierte T-Zellen konnten intratumoral in einem murinen Gliommodel mittels 9.4 Tesla MRT mit hoher Sensitivität dargestellt und über einen Zeitraum von mindestens zwei Wochen verfolgt werden. Relaxatationszeiten des Tumors zu einem frühen Zeitpunkt nach adoptivem Zelltransfer korrelierten mit Tumoransprechen oder -resistenz, was zeigt, dass nicht-invasive Quantifizierung von räumlichen und zeitlichen T-Zell-Dynamiken im Tumormikromilieu als Prädiktor für den Erfolg von individuellen Immuntherapien fungieren können.

Introduction

Immunosuppressive tumor microenvironment in glioma

Gliomas are primary brain tumors with a high malignancy and poor median overall survival of 12-15 months.[1–3] They are the most common primary tumors of the central nervous system (CNS). Adult-type diffuse gliomas include IDH-mutant oligodendroglioma and astrocytoma as well as isocitrate dehydrogenase (IDH)-wildtype glioblastoma (GBM).[4] Treatment options for gliomas including GBMs are limited and standard of care consists of surgical resection, radiotherapy as well as chemotherapy with the alkylating agent temozolomide.[5] Due to the invasiveness of glioma cells into the healthy brain, complete resection is difficult to achieve and there is a high rate of tumor recurrence that is often accompanied with additional acquired molecular changes. While immunotherapy has improved patient outcome for multiple solid tumor entities including non-small-cell lung cancer and melanoma[6,7], immunotherapeutic approaches such as immune checkpoint blockade (ICB) have shown heterogeneous responses in preclinical glioma studies[8,9], but did not prove to be effective against gliomas in clinical trials due to a lack of a survival advantage.[10–12] Gliomas exhibit a highly immunosuppressive tumor microenvironment (TME), characterized by a large number of anti-inflammatory tumor-associated macrophages (TAMs) as well as poor T cell infiltration into the tumor and additionally increased T cell exhaustion.[13–15] T cell exhaustion is characterized by upregulation of checkpoint receptors like programmed cell death protein 1 (PD-1) or cytotoxic T-lymphocyte-associated Protein 4 (CTLA-4), surface receptors on T cells, which physiologically fulfil the role of downregulation of T cell activation in order to prevent autoimmune reactions, but limit T cell function necessary for tumor eradication. They are therefore of disadvantage during tumor surveillance. Hence, immunotherapies aim to inhibit checkpoint receptors, decrease overall T cell exhaustion and induce tumor eradication.

The T cell compartment of lymphocytes include T helper cells (CD4+ T cells), cytotoxic T cells (CD8+ T cells) and regulatory T cells (Tregs). While T cells are hardly present in the healthy brain, inflammatory processes in the CNS can lead to a disrupted blood brain barrier (BBB) that facilitates recruitment of T cells from the periphery to the brain[16,17]. CD8+ T cells can recognize tumor-antigens via the T cell receptor (TCR) when interacting with antigen-presenting cells such as dendritic cells or macrophages, which present processed tumor-antigens on human leucocyte antigen 1 (HLA1) or the murine homologue major histocompatibility complex I (MHCI). Upon recognition of tumor-antigen, $CD8^+$ T cells secrete cytokines such as interferon γ (IFNγ) as well as tumor necrosis factor α (TNFα) and cytotoxic granules, which can lead to killing of the tumor cells (figure 1). $CD8^+$ T cells therefore play a major role in cancer immunosurveillance; tracking of T cell recruitment and distribution could hence help understand mechanisms of resistance. Due to their cytotoxic function and direct anti-tumor effect, this project focuses on $CD8^+$ T cells. It has been shown that chronic antigen exposure results in T cell exhaustion due to increased expression of immune checkpoints, decreased effector function after TCR stimulation and lower proliferative capacity.[18–20] T cell exhaustion and hence upregulation of immune checkpoints are therefore subject for therapeutic intervention.

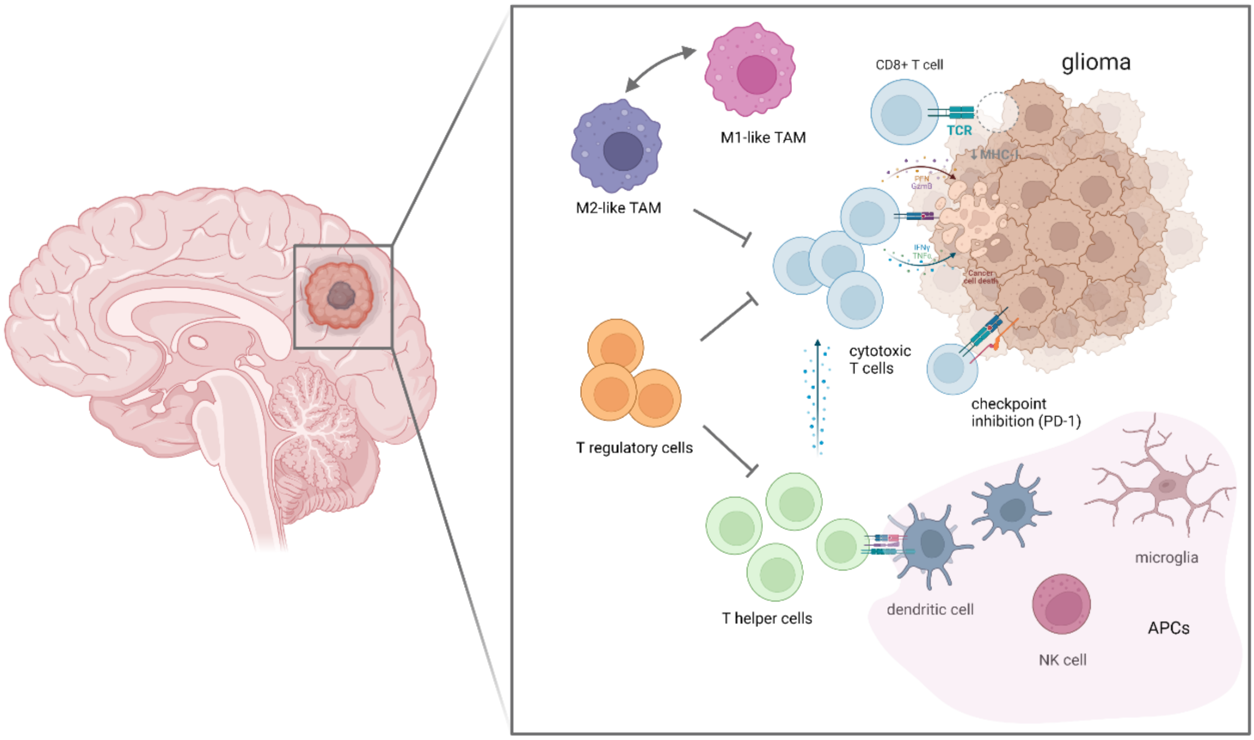

Figure 1: Immunosuppressive TME in glioma

Schematic visualization of T cells, macrophages, antigen-presenting cells (dendritic cells, NK cells and microglia) and their interaction in the tumor microenvironment in glioma, created with Biorender

Immunotherapies in glioma treatment

In order to target immune checkpoints, checkpoint inhibitors such as anti-PD1 and anti-CTLA4 antibodies have been developed. In contrast to chemo- and radiotherapy, which are based on non-specific targeting of proliferating cells, checkpoint inhibitors modulate immune cells and are therefore not accompanied by side effects like fatigue and hair loss that a majority of patients experience with chemotherapy. In adoptive cell therapy (ACT), patient-derived T cells are engineered with a tumor-specific TCR and injected intravenously (figure 2). ACT is therefore a therapeutic approach that could be individualized for each patient based on the antigen expression of the respective tumor and could furthermore be combined with ICB. Neoantigen occurrence in gliomas is low, therefore gliomas are considered “immunologically cold tumors” with few targetable tumor-specific mutations. This complicates the search for effective TCRs. Intratumoral heterogeneity regarding antigen expression further complicates treatment.[21]

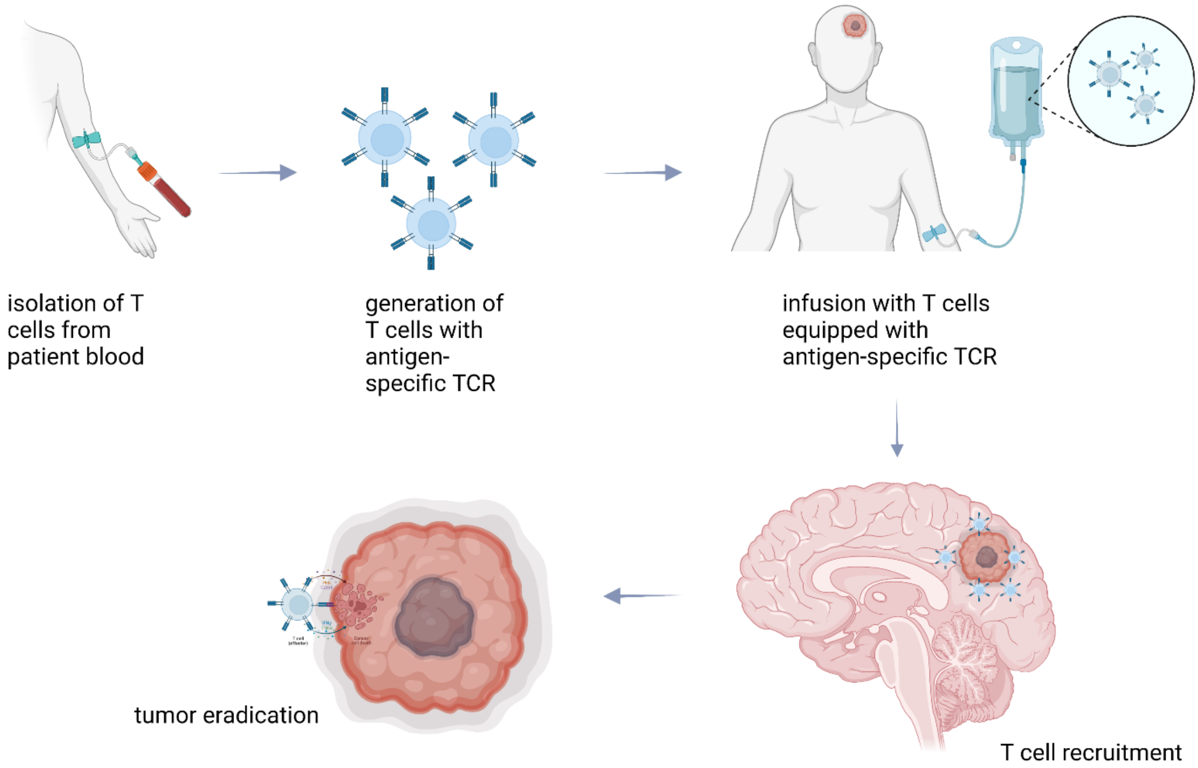

Figure 2: Adoptive T cell transfer

Schematic visualization of adoptive T cell transfer with antigen-specific TCR in patients, created with biorender: T cells are isolated from a patient’s blood and genetically engineered with a tumor antigen-specific TCR; the engineered T cells are then infused into the patient and recruited to the tumor where they can recognize and eradicate the tumor

Other immunotherapies include the use of chimeric antigen receptor (CAR) T cells or peptide and mRNA vaccinations.[5] CAR T cells are engineered T cells that combine T cell binding and T cell activating features: They contain an extracellular single-chain variable fragment (scFv) and a transmembrane domain in addition to an intracellular region of immunoreceptor tyrosine-based activation motifs (ITAMs) associated with a co-stimulation.[22] They bind to unprocessed antigens expressed on the cell surface instead of targeting processed peptides presented by MHC molecules. Compared to TCRs, CARs have a higher affinity, but lower sensitivity.[23,24] A promising example for CAR T cell therapy are CD19 CARs that have been FDA approved for the treatment of certain types of lymphomas and leukemias.[25] For the treatment of glioblastoma, infusions with CAR T cells targeting the IL-13 receptor α2 into the resected tumor cavity combined with intraventricular infusions lead to tumor regression in a single patient and was well tolerated by other patients.[26,27] In addition, CAR T cell therapy targeting the disialoganglioside GD2 in H3K27M-mutated gliomas showed clinical benefit in three out of four patients in a phase I study.[28] However, a clinically approved CAR therapy is still missing in the treatment of gliomas.[29,30]

An additional target for immunotherapy in glioma are TAMs.[31] Macrophages in the TME can be classified into pro-inflammatory (also called M1-like) and anti-inflammatory (also called M2-like) phenotypes that can act anti- or protumorigenic, respectively and influence T cell activity.[32,33] However, macrophage phenotypes in the TME occur with a broad heterogeneity of TAMs *in vivo* rather than clear M1/M2 dichotomy as previously assumed by *in vitro* studies.[34] Immunotherapies targeting macrophages such as R848-loaded β-cyclodextrin nanoparticles (CDNP-R848) that acts as a toll like receptor (TLR) 7/8 agonist aim to shift the phenotype of TAMs towards a more pro-inflammatory and anti-tumorigenic phenotype.[35] Turco et al. have shown that treatment with CDNP-R848 leads to tumor regression in a preclinical glioma model.[36]

However, response to immunotherapy is very heterogeneous in preclinical research as well as in clinical trials, especially in solid cancer entities.[8,37] Mechanisms of resistance are largely unknown. Currently, no immunotherapy is clinically approved for the treatment of glioma. Even in genetically identical mouse models, treatment with checkpoint inhibitors or CAR T cells leads to responders, non-responders and the phenomenon of pseudoprogression.[38] During pseudoprogression, an initial mass increase is detectable by magnetic resonance imaging (MRI) despite of therapy response, which is presumably caused by immune cell influx. Tumor growth and tumor mass enlargement due to immune cell infiltration as seen in pseudoprogression can often not be differentiated by conventional MRI.[39,40] The ability to differentiate tumor mass enlargement caused by immune cell infiltration from actual tumor growth by non-invasive visualization of immune cells would therefore be beneficial for therapy evaluation. T cell recruitment to the TME, intratumoral immune cell distribution as well as T cell activity are likely a major determinant for the efficacy of immunotherapies. This creates the need for non-invasive treatment monitoring so that therapy outcome can be predicted and adapted accordingly. Currently, non-invasive, cellular treatment monitoring of immunotherapies is not available in glioma.

Magnetic resonance imaging

MRI is commonly used as a diagnostic tool for tumor growth monitoring and response assesment in clinical practice is based on response assessment for neuro-oncology (RANO) criteria.[41] There are efforts to advance MRI to cellular imaging in order to enable visualization of specific cell populations such as immune cells. Iron can be visualized by MRI since it reduces the relaxation time, which is visible as hypointense signal. T2 is the transversal relaxation, also called spin-spin relaxation time, in which spin relaxation time is measured after the application of a radiofrequency pulse.[42] While tumor volumes are visualized by T2-weighted/FLAIR images or on T1-weighted images after the application of Gadolinium contrast agents, visualization of iron can be performed using T2*/multi-gradient echo (MGE), which detects magnetic inhomogeneities within the tissue. Based on the MGE, relaxation times can be calculated, which represent the time needed for proton spins to return to their initial magnetization after the application of the radiofrequency pulse. Previous reports have shown that immune cells can be labeled and visualized by MRI using iron oxide nanoparticles (NP).[43,44] In addition to MRI, positron emission tomography (PET) combined with a computed tomography scan (CT) represents another diagnostic modality used especially in oncology that has shown potential for visualization of immune cells using cell specific radiotracers. In contrast to MRI, PET detects positron-emitting radiopharmaceuticals in order to generate a three-dimensional map and requires administration of a radioactive tracer. CT is an X-ray based imaging technique. The combination of both allows for the merging of physiological and morphological properties.

Since recruitment of T cells to the tumor microenvironment and distribution of T cells within the tumor might be a major determinant for the efficacy of immunotherapies, this dissertation focuses on the non-invasive tracking of T cells to the TME in a murine glioma model in order to monitor and predict treatment outcome. I hypothesized that T cells can be visualized intratumorally and that responders and non-responders to immunotherapy can be differentiated at an early time point based on T cell infiltration and distribution.

Results

NP labeling does not affect T cell viability or functionality

For the visualization of T cells by MRI, I used the commercially available NP Molday ION Biopal Evergreen with the formula Fe3O4 [C6H10O5]n conjugated to FITC, which contains 2 mg Fe/ml. It is an iron-based ultrasmall superparamagnetic nanoparticle (USPIO) with a mean particle size of 35 nm, a magnetite core with a size of 8 nm and a dextran coating (figure 3A). Moreover, the NP has a fluorescent tag that can be detected by flow cytometry and confocal microscopy. In a first step, I assured that the iron oxide NP itself can be visualized and quantified by MRI in a T2* sequence using a high field 9.4 Tesla experimental MRI scanner. The multi-echo gradient-echo (MGE) sequence detects magnetic field inhomogeneities and is therefore suited for the imaging of iron oxide NP. Different concentrations of NP diluted in PBS were measured and based on the MGE, T2* maps were calculated to quantify the relaxation time for each voxel. The T2* relaxation time was correlated with the amount of iron (figure 3C). Figure 3 shows that the PBS control has a relaxation time of 129 ms, while the NP reduces the relaxation time with 20 µg Fe resulting in 18 ms and 40 µg Fe resulting in a very short relaxation time of 9 ms. Iron was visible as hypointense spots due to the reduction of the relaxation time (figure 3B).

In order to visualize T cells using this iron oxide NP, I firstly analyzed whether labeling of T cells with the NP was possible. T cells were incubated with 25 µl/ml NP for 24 h *in vitro* with the addition of interleukin 2 (IL-2), a T cell growth factor which enhances T cell differentiation and is needed for T cell proliferation. Labeling efficiency was assessed using flow cytometry based on the Evergreen fluorescence of the NP that can be detected in the FITC channel (figure 4A). After 24 h, a labeling efficiency of

>99% was achieved *in vitro* (figure 4B). Labeling efficiency remained at >99% after 48 h and after seven days in *vitro*, 73 % of T cells were on average still NP-labeled, which indicates that long-term labeling of T cells with the NP is possible. Intracellular localization of the NP was furthermore confirmed by confocal microscopy comparing unlabeled T cells with NP labeled T cells (figure 4C). In addition, subcellular localization of the NP was assessed by transmission electron microscopy (TEM), figure 4D, which revealed localization of the NP in vesicles.

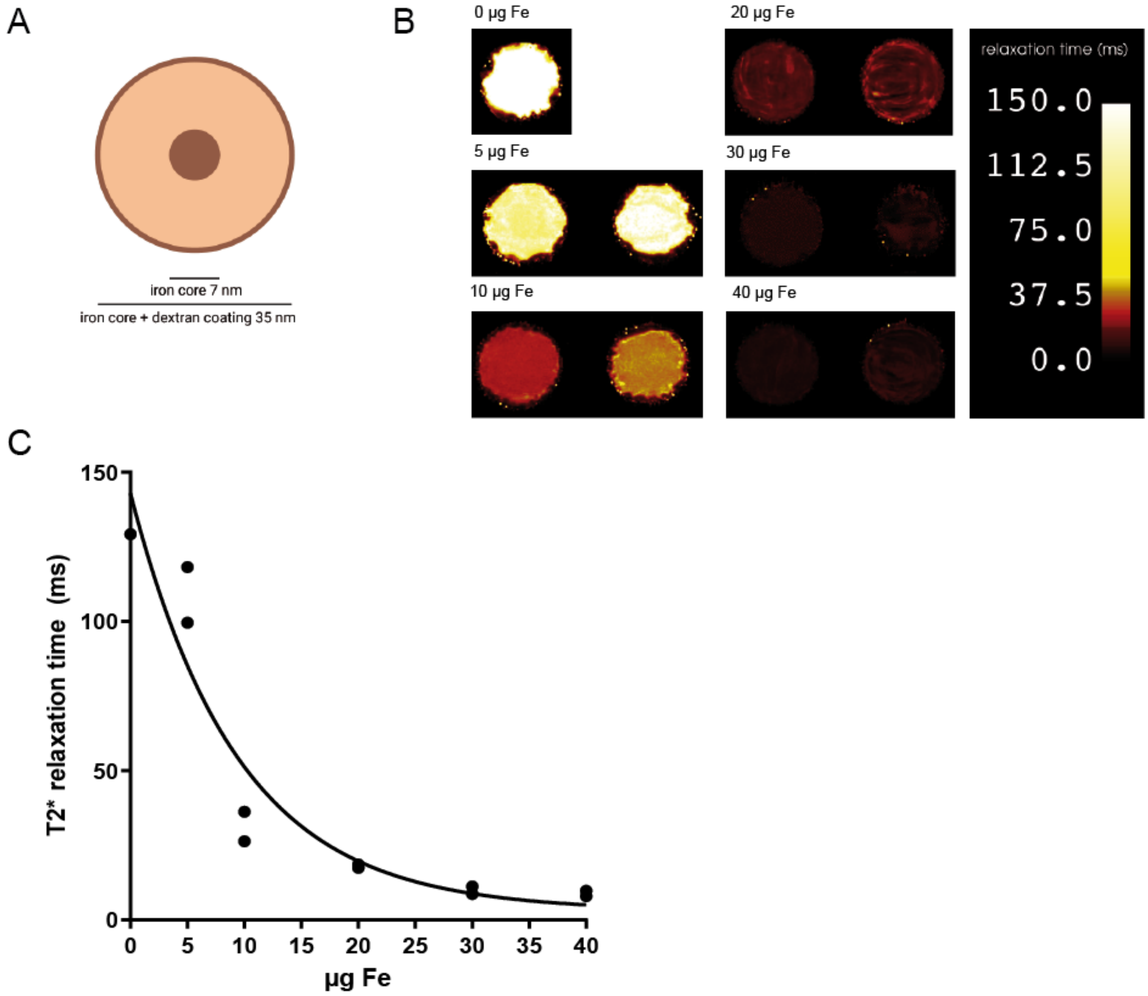

Figure 3: Molday ION BioPAL iron oxide NP can be visualized by T2* mapping

A schematic structure of Molday ION BioPAL iron oxide nanoparticle **B** T2*maps of 0 - 40 µg Fe measured by 9.4 Tesla MRI **C** quantification of T2* relaxation times, correlation of T2* relaxation times and iron content

With the aim of assessing the NP uptake and therefore the iron concentration per cell, inductively coupled plasma optical emission spectrometry (ICP-OES) was performed. The incubation with 5, 25, 50 and 100 µg Fe/1x10^6 cells resulted in an average uptake of 1.0 pg Fe/cell, 1.8 pg Fe/cell, 2.3 pg Fe/cell and 3.0 pg Fe/cell, respectively (figure 4E). The iron uptake per cell therefore correlates with the amount of added NP and resembles a saturation curve. The incubation with 100 µg Fe does not lead to saturation, but is likely close to saturation. Given the saturation curve, an addition of more NP would likely only minorly increase the intracellular iron concentration, while potentially increasing the toxicity on the T cells, which is why the following experiments were continued with T cells labeled with around 2.3 pg Fe/cell. NP uptake by macrophages, which have the ability to perform phagocytosis, was used in comparison. ICP-OES measurements of NP labeled macrophages showed that macrophages took up a similar amount of Fe/cell as T cells (figure 4F).

T cells labeled with 2 pg Fe/cell were tested for their viability and functionality such as cytokine secretion and antigen-specific killing activity. Viability of labeled T cells did not differ from viability of unlabeled T cells at any time point (24 h, 48 h or seven days) (figure 5A). IFN γ secretion was assessed by incubation with the calcium ionophore ionomycin, which stimulates vesicle release, PMA and the endoplasmic reticulum (ER)-Golgi transport inhibitor brefeldin A. The secretion of IFN γ was not affected by NP labeling *in vitro* in comparison to unlabeled T cells (figure 5B). Antigen-specific killing activity was assessed via lactate dehydrogenase (LDH) release assay via co-incubation of Gl261-Ova and the respective antigen-specific OT-1 T cells. The Gl261 cell line was chosen since it is a well characterized syngeneic mouse glioma model that was created by chemical carcinogenesis and contains activating mutations of K-Ras and the tumor suppressor p53.[45]

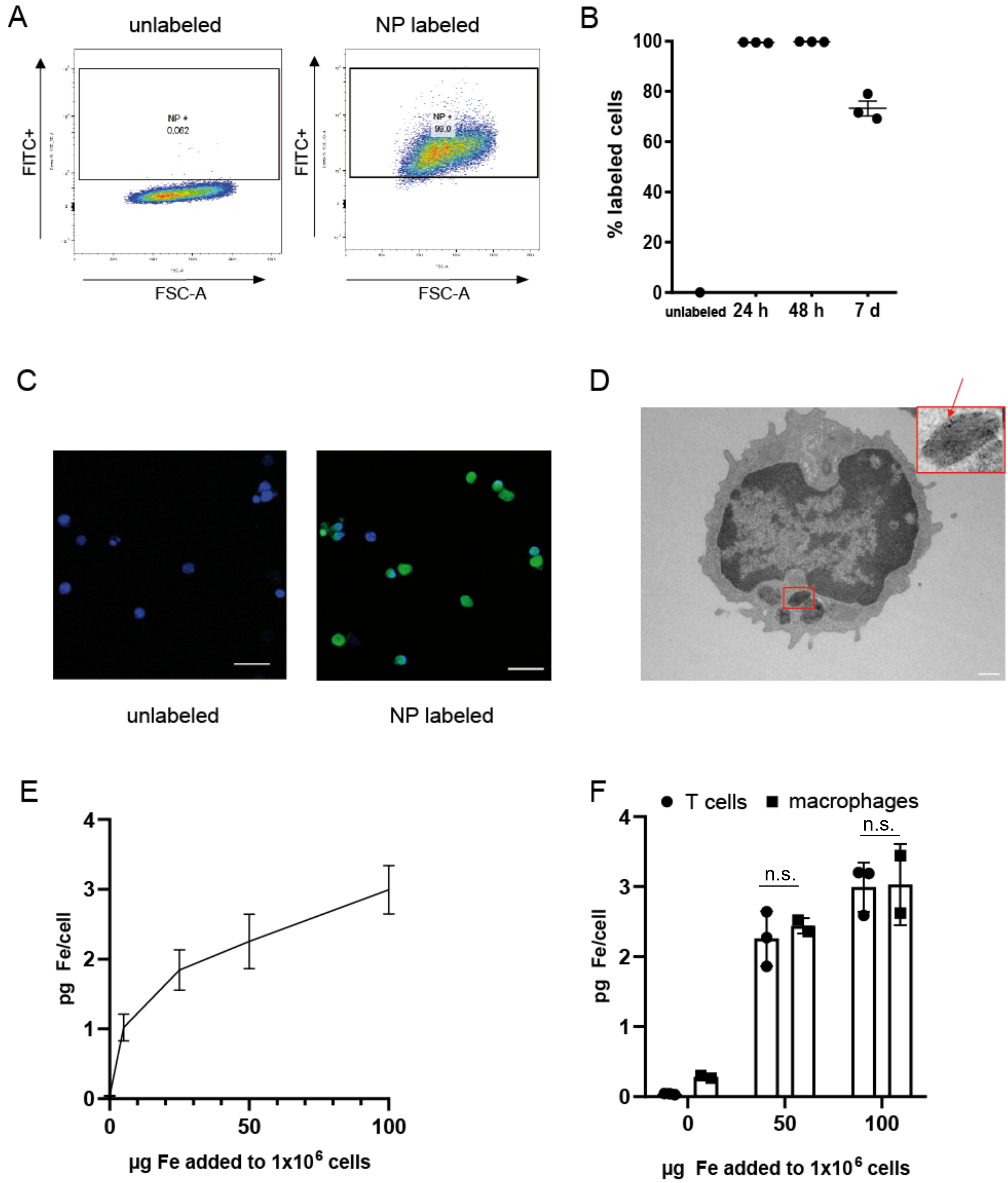

Figure 4: Primary murine T cells can be labeled with iron oxide NP

A Flow cytometry plots of unlabeled vs. iron oxide NP labeled T cells **B** Iron oxide NP labeling efficacy of T cells after 24 h, 48 h and 7 d assessed by flow cytometry **C** Confocal images of unlabeled and NP labeled T cells, blue = DAPI, green = FITC channel, scale = 20 µm **D** Transmission electron microscopy image of iron oxide NP labeled T cells, scale bar = 500 nm, arrow indicates location of NP, TEM images were acquired in cooperation with Rachel Santarella-Mellwig **E** Intracellular Fe concentration of T cells after 24 h incubation with iron oxide NP, analyzed by ICP-OES **F** Comparison of intracellular Fe concentration of T cells vs. macrophages after 24 h incubation with iron oxide NP, macrophages were provided by the research group of Prof. Martina Muckenthaler, Otto-Meyerhof-Zentrum. Data are displayed as mean ± SD.

Therefore, the Gl261 cell line is commonly used in pre-clinical glioma research and is a suitable model for the tracking of immune cell recruitment in the glioma TME. The LDH assay used to assess antigen-specific killing activity of NP labeled T cells is based on the release of LDH from the plasma of target cells, which resembles plasma membrane damage and allows inference regarding the cytotoxicity in co-culture assays. The LDH assay showed slightly decreased killing activity of NP labeled T cells compared to unlabeled T cells (figure 5C). Incubation of either labeled or unlabeled OT-1 T cells with tumor cells lacking the Ova-antigen did not result in cytotoxicity, which confirms that the observed cell death is indeed based on antigen-specific killing activity. Following up on these results, a real-time cell analysis (RTCA) assay was performed to further study the antigen-specific killing activity of NP labeled T cells. The method allows monitoring of tumor cell adhesion based on microsensor electrodes and therefore enables assessment of cytotoxicity. Coculture of Gl261-Ova and OT-1 T cells, comparing killing activity of unlabeled vs. NP labeled T cells, did not show any evidence for reduced antigen-specific killing activity of NP labeled T cells (figure 5D). Consequently, even if the antigen-specific killing activity of NP labeled T cells was slightly reduced as indicated by the LDH release assay, NP labeled T cells are still able to sufficiently kill target cells in an antigen-specific manner.

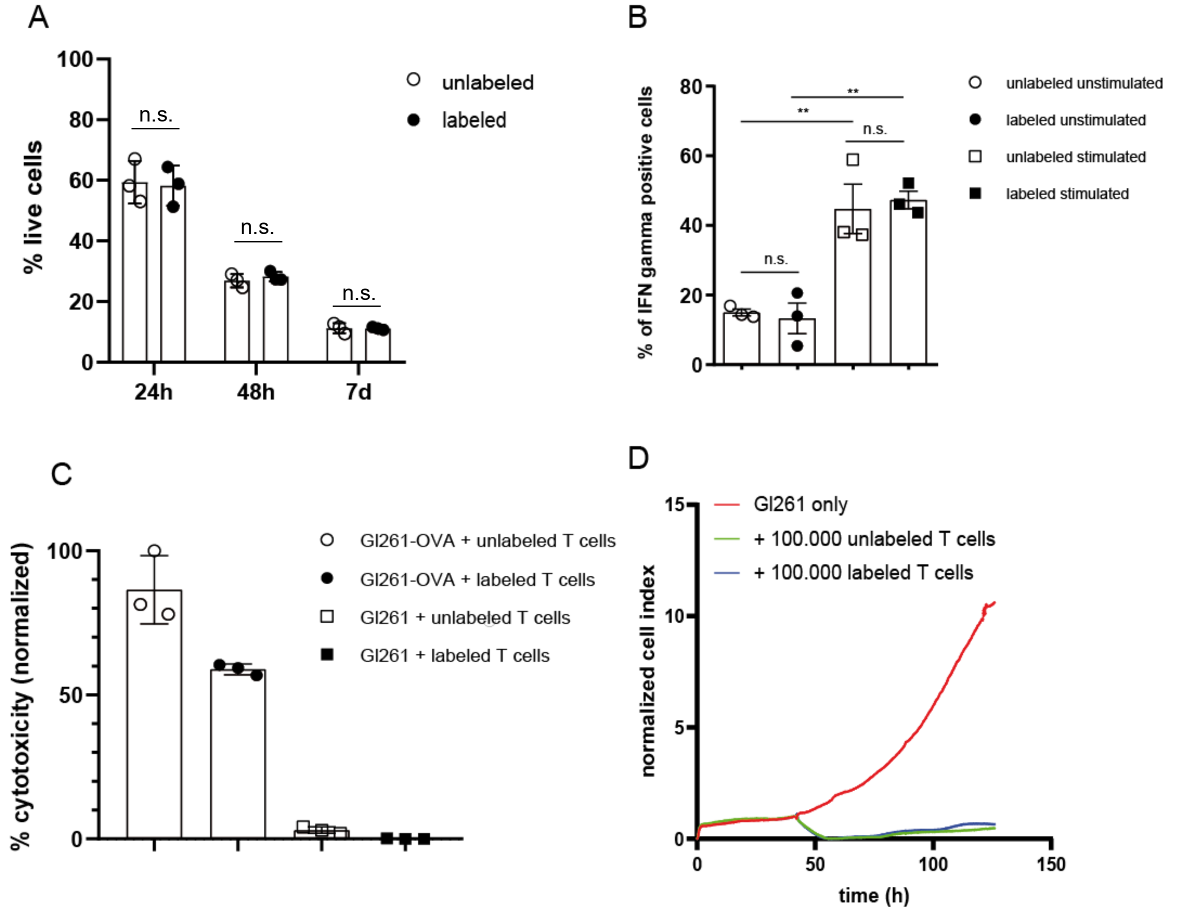

Figure 5: Iron oxide NP labeling does not affect T cell viability or functionality

A viability of iron oxide NP labeled vs. unlabeled T cells at 24 h, 48 h and 7 d *in vitro*, asessed by flow cytometry **B** IFN γ secretion of NP labeled vs. unlabeled murine T cells, assessed by flow cytometry **C** LDH release assay comparing antigen-specific killing activity of iron oxide NP labeled T cells vs. unlabeled T cells in coincubation with Gl261-Ova cells and Gl261 control cells **D** RTCA of iron oxide NP labeled T cells vs. unlabeled T cells. Data are displayed as mean ± SD.

NP labeled T cells can be detected by MRI with high sensitivity

In order to assess MRI sensitivity and feasibility of visualization, different amounts of iron oxide NP labeled T cells (100, 1,000 and 10,000) were injected intracranially in healthy mice and compared to unlabeled T cell injections (figure 6A). Relaxation times of injection sites were quantified and normalized to healthy brain tissue, respectively. Injection of 10,000 NP labeled cells lead to a significant reduction of relaxation time compared to unlabeled cells (figure 6B). Injection of 10,000 labeled T cells was furthermore clearly visible on the MR images due to the hypointense spot based on the reduced relaxation time (figure 6C). Therefore, NP labeled T cells can be detected with a high sensitivity by MRI in a mouse brain with a detection limit at around 10,000 cells.

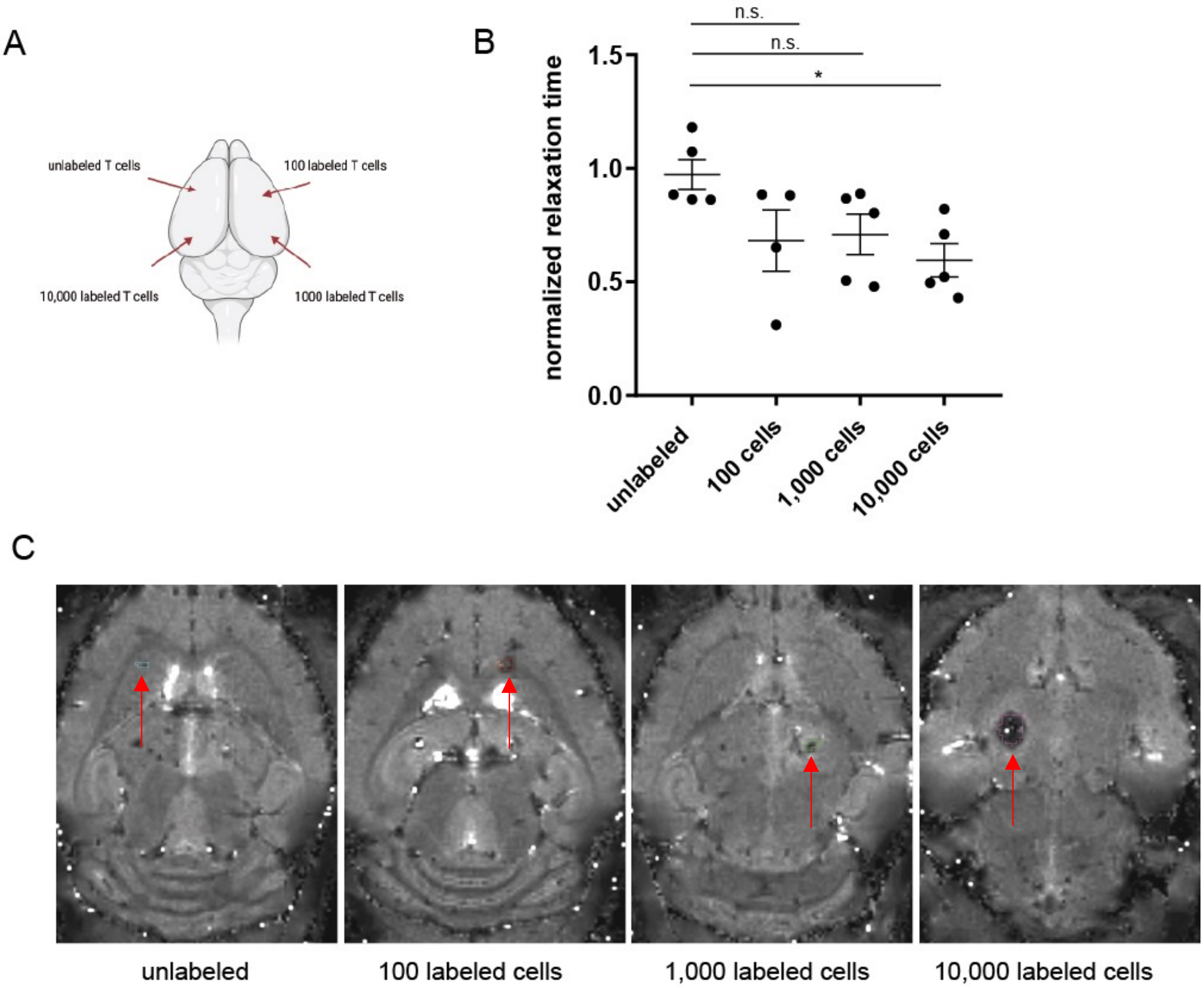

Figure 6: Iron oxide NP labeled T cells can be detected with high sensitivity by MRI

A schematic overview of injection sites of 100, 1000 or 10,000 NP labeled T cells in a mouse brain **B** quantification of T2* relaxation times of 10,000 unlabeled or iron oxide NP labeled T cells (100, 1000, 10,000 cells) normalized to healthy brain tissue, displayed as mean ± SD, statistical significance assessed by one-way ANOVA **C** T2* maps of intracranial T cell injection sites, arrows and segmentations indicate injection sites

In vivo T cell tracking

For *in vivo* T cell tracking, the Gl261-GP100 model was used. GP100 is a highly glycosylated protein naturally expressed in melanoma cells that was expressed in Gl261 cells in order to function as an antigen for PMEL T cells, which carry a rearranged T cell receptor transgene specific for GP100. Once tumors were established, antigen-specific PMEL T cells were labeled with the NP *in vitro* and labeling efficiency was assured by flow cytometry. 1×10^6 T cells were injected intratumorally on day 12 after tumor inocculation (figure 7A). MRI measurements were performed one and three days after ACT. Quantification of the tumor area revealed a significant decrease in relaxation time of labeled T cell injections compared to unlabeled T cell injections that was detectable after one day as well as after three days (figure 7B). Reduced relaxation time at the tumor border suggests that adoptively transferred T cells might be located in the tumor border rather than in the tumor core (figure 7C). Immunohistochemical (IHC) analysis showed that adoptively transferred PMEL T cells are restrained to the tumor area and are not evenly distributed within the tumor, as also suggested by MRI data (figure 7D). FITC/Evergreen fluorescence of the NP is quenched over time *in vivo* and flow cytometry analyses were therefore inconclusive as a readout for intracellular NP labeling. However, Prussian blue staining showed iron within the tumor area overlapping with the $CD90.1^+/CD3^+$ co-staining of PMEL T cells and also correlating with the areas of reduced relaxation time on MRI, which provides evidence that the NP is indeed still located intracellularly in the adoptively transferred T cells and that the MRI signal is specific for these T cells (figure 7D).

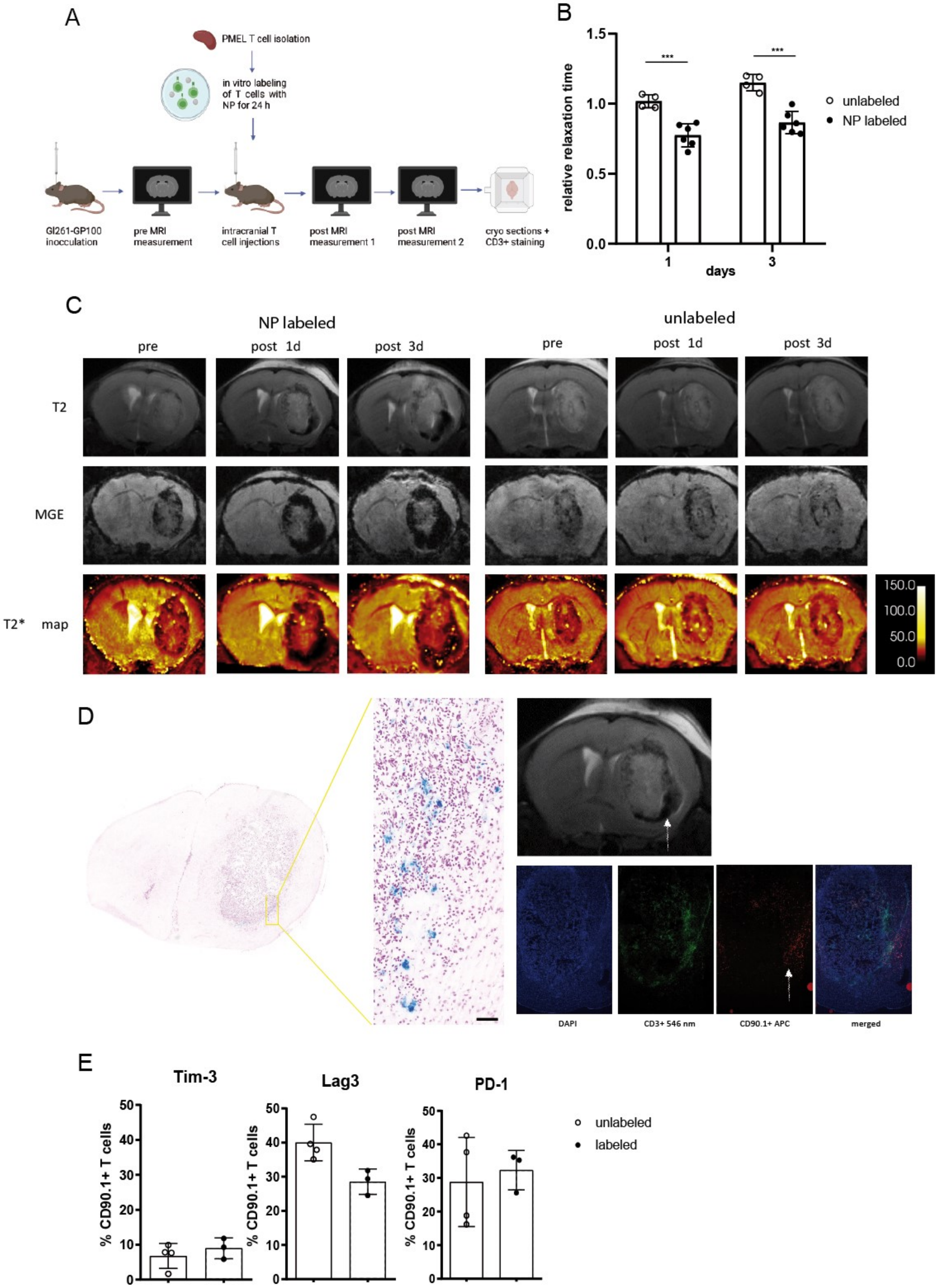
A
PMEL T cell isolation
in vitro labeling of T cells with NP for 24 h
Gl261-GP100 inocculation
pre MRI measurement
intracranial T cell injections
post MRI measurement 1
post MRI measurement 2
cryo sections + CD3+ staining
B
relative relaxation time
1.5
1.0
0.5
0.0
***
***
1
3
days
○ unlabeled
● NP labeled
C
NP labeled
unlabeled
pre
post 1d
post 3d
pre
post 1d
post 3d
T2
MGE
T2* map
150.0
100.0
50.0
0.0
D
DAPI
CD3+ 546 nm
CD90.1+ APC
merged
E
Tim-3
Lag3
PD-1
% CD90.1+ T cells
50
40
30
20
10
0
○ unlabeled
● labeled

Figure 7: Iron oxide NP labeled T cells can be visualized intratumorally by MRI

A experimental time line **B** quantification of T2* map relaxation times of tumor area one and three days after ACT, in relation to pre measurement, displayed as mean ± SD **C** T2, MGE and T2* map of a representative animal that received unlabeled or NP labeled T cells **D** Prussian blue staining of mouse brain after iron oxide NP ACT next to the respective MRI and $CD3^+/CD90.1^+$ co-staining, imaged by confocal microscopy, scale bar = 50 µm **E** T cell exhaustion markers comparing unlabeled and iron oxide NP labeled T cells after ACT, data are displayed as mean ± SD

For the purpose of analyzing T cell function after NP labeling *in vivo*, T cell exhaustion markers PD-1, T cell immunoglobulin and mucin domain-containing protein 3 (Tim-3) and lymphocyte-activation gene 3 (Lag3) were analyzed in PMEL T cells 8 days after ACT. No significant difference in exhaustion marker expression was detected between unlabeled and NP labeled adoptively transferred T cells (figure 7E).

After this successful establishment of the method, other, more clinically relevant T cell injection routes were tested for non-invasive T cell tracking. Intraventricular injections were performed in a similar fashion to the intratumoral injections, however, MRI measurements were performed two and four days after ACT to allow for T cell migration from the ventricle to the tumor. Quantification of the ventricle showed a significant reduction of relaxation time of labeled T cell injection compared to unlabeled T cell injection, which means that a visualization of NP labeled T cells within the ventricle is possible (figure 8A + 8B). However, T cells seemed to have remained stationary within the ventricle and did not migrate from the ventricle to the tumor as relaxation time of tumor area was not changed (figure 8C). IHC confirmed that no PMEL T cells were found in the tumor area, but in proximity to the ventricle. For intravenous injections, ACT of NP labeled T cells was accompanied by irradiation of 2 x 2 Gy to increase T cell infiltration of the tumor. Flow cytometry showed an infiltration of very few adoptively transferred T cells in the tumor hemisphere after two days (figure 8D). Quantification of the tumor area subsequently did not show a difference in relaxation time comparing pre and post ACT measurements. Hence, as also seen for intraventricular injections in the Gl261-GP100 model, there was not sufficient PMEL T cell recruitment to the tumor for detection by MRI. In line there was no anti-tumor effect observed. Based on these results, the Gl261-GP100 model seemed not to be a suitable model for to further establish non-invasive T cell tracking and I switched to the Gl261-Ova model. In this model, the ovalbumin peptide that orginates from chicken eggs is expressed in Gl261 cells and can be recognized by ovalbumin-specifc CD8$^+$ T cells (OT-1 T cells).

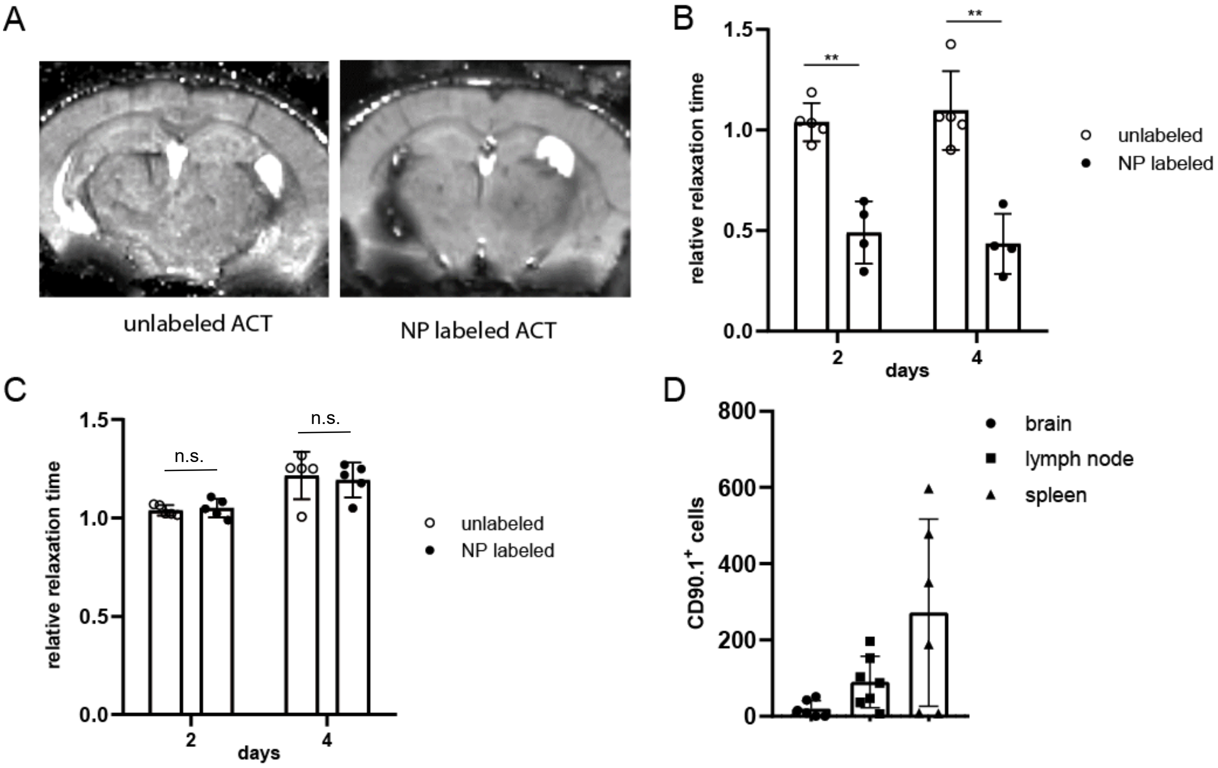

Figure 8: Alternative injection routes for iron oxide NP labeled ACT

A T2* maps of intraventricular ACT comparing unlabeled and iron oxide NP labeled T cell injection **B** quantification of T2* maps of ventricles after intraventricular ACT after 2 and 4 days comparing unlabeled and iron oxide NP labeled T cells **C** quantification of T2* maps of tumor area after intraventricular ACT after 2 and 4 days **D** PMEL T cell infiltration after i.v. ACT in brain, lymph node and spleen, quantified by flow cytometry. Data are displayed as mean ± SD

Low relaxation time of tumor area at an early time point correlates with partial or complete tumor response at end time point

Having shown that visualization and quantification of T cells in a murine glioma model by MRI is possible, the goal was to assess the feasibility of tracking adoptively transferred T cells over a longer period of time and furthermore to correlate T cell distribution with tumor response criteria. Mice with Gl261-Ova tumors received iron oxide NP labeled, antigen-specific OT-1 T cells intratumorally and were monitored by MRI 3, 7, 10 and 14 days after ACT. Figure 9 shows that long-term tracking of T cells over a period of at least two weeks is possible and that the reduced relaxation time caused by adoptively transferred T cells is still visible after this prolonged time period. In some mice, the T cells seemed to redistribute within the tumor over time, while in others the T cells seemed to be stationary (figure 9A). Tumor response was classified as progressive disease (PD), stable disease (SD), partial response (PR) and complete response (CR) as previously established by Aslan et al and based on iRANO.[8] Relaxation times after ACT of tumor areas were quantified based on T2*maps and normalized to relaxation times before ACT (pre MRI), since baseline relaxation times slightly vary between mice. Upon classifying tumor response according to the tumor response criteria, it became apparent that those with a low mean relaxation time (>0.6) of the tumor area at an early time point (d3 after ACT) developed a partial or complete response, while mice with a high mean relaxation time of the tumor at an early time point did not respond and showed progressive or stable disease (figure 9B). These results could be repeated in a second, independent experiment that also showed that a low tumor relaxation time at an early time point after ACT predicts tumor regression, while a high mean relaxation time of the tumor area is an indicator for tumor immune escape. Mice that received intratumoral PBS injections or no injections at all were used as control. PBS injections did not change the relaxation time compared to the pre MRI measurement (figure 9B). When no injections were performed, tumors continued to grow. However, the injection of PBS led to a tumor regression in some of the animals. This phenomenon is likely due to the spontaneous activity of endogenous T cells in this very immunogenic glioma model, which cannot be visualized non-invasively in my NP imaging approach.

$CD3^+$ staining in cleared brains correlates with reduced relaxation times detected by MRI

For the purpose of providing further evidence that the detected MRI signal actually stems from NP labeled, adoptively transferred T cells, whole mouse brains were cleared post-mortem and light sheet microscopy was correlated with MRI datasets. The Gl261-Ova model with intratumorally injected, NP labeled OT-1 T cells was used for this purpose. OT-1 T cell distribution was tracked non-invasively by MRI and whole mouse brains were afterwards processed for tissue clearing using immunolabeling-enabled three-dimensional imaging of solvent-cleared organs (iDisco) with a $CD3^+$ staining in order to obtain a 3D model of T cell infiltration. Tissue clearing renders the sample transparent by minimization of the refractive index differences, which includes the removal of lipids. This allows deep imaging of the tissue that would normally be limited by the scattering of light within the tissue. Figure 10 shows the distribution of $CD3^+$ cells. Location of the T cells in the light microscopy data correlates with areas of reduced relaxation time detected by MRI. T cell localization on the tumor border or a rather homogenous T cell distribution within the tumor that can be seen in the cleared brains is also detectable by MRI. This serves as additional evidence that hypointense signal visible by MRI correlates with T cell localization.

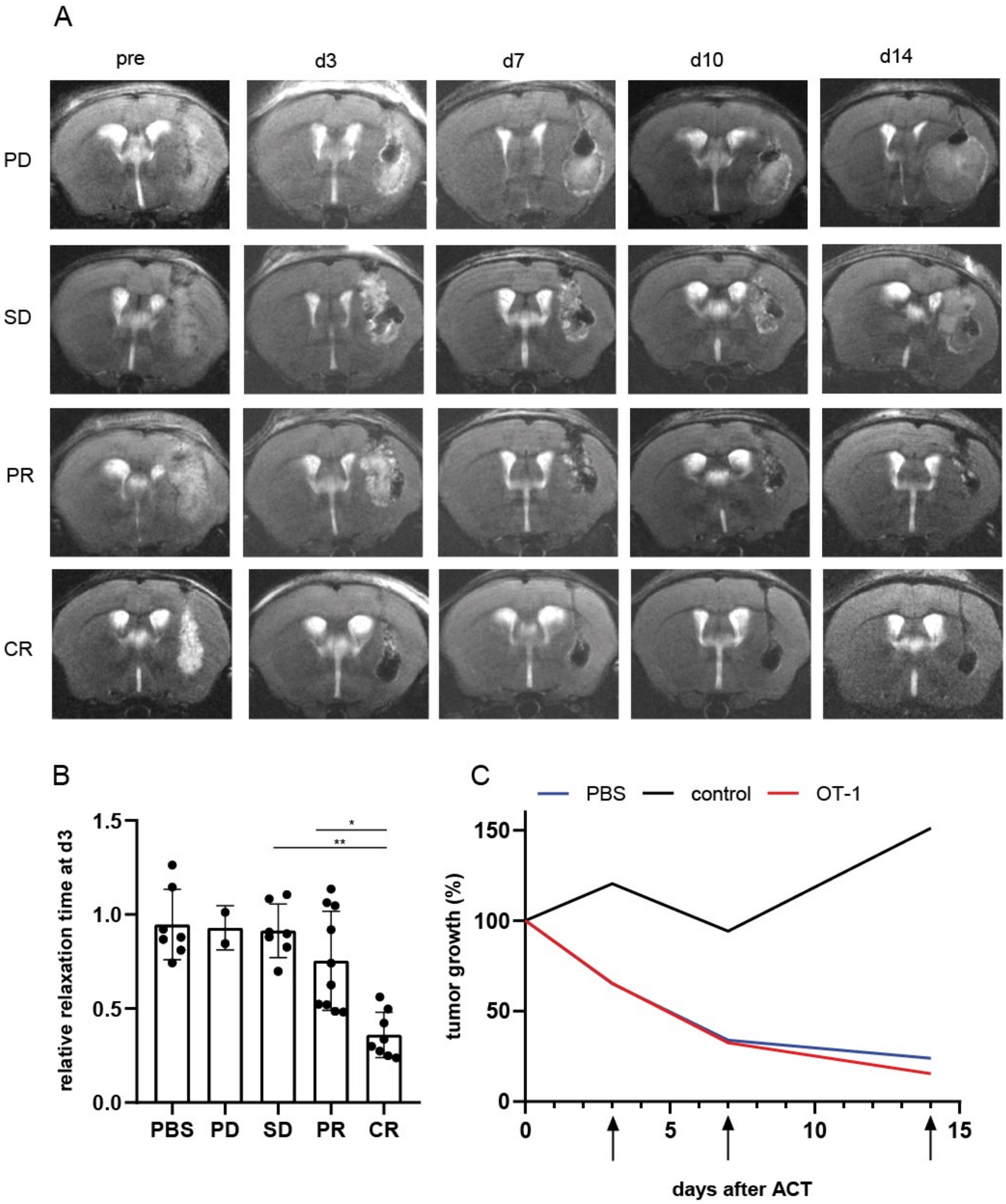

Figure 9: Tumor relaxation times can function as predictor for response and resistance after iron oxide NP labeled ACT

A MR images of Gl261 tumors after intratumoral ACT, PD = progressive disease, SD = stable disease, PR = partial response, CR = complete response **B** Quantification of T2* map relaxation times of tumor area 3 days after intratumoral ACT of iron oxide NP labeled T cells, displayed as mean ± SD, statistical significance assessed by one-way ANOVA **C** Tumor growth curve of PBS, OT-1 T cell and control cohort (no intervention), arrows indicate time points of MRI measurements

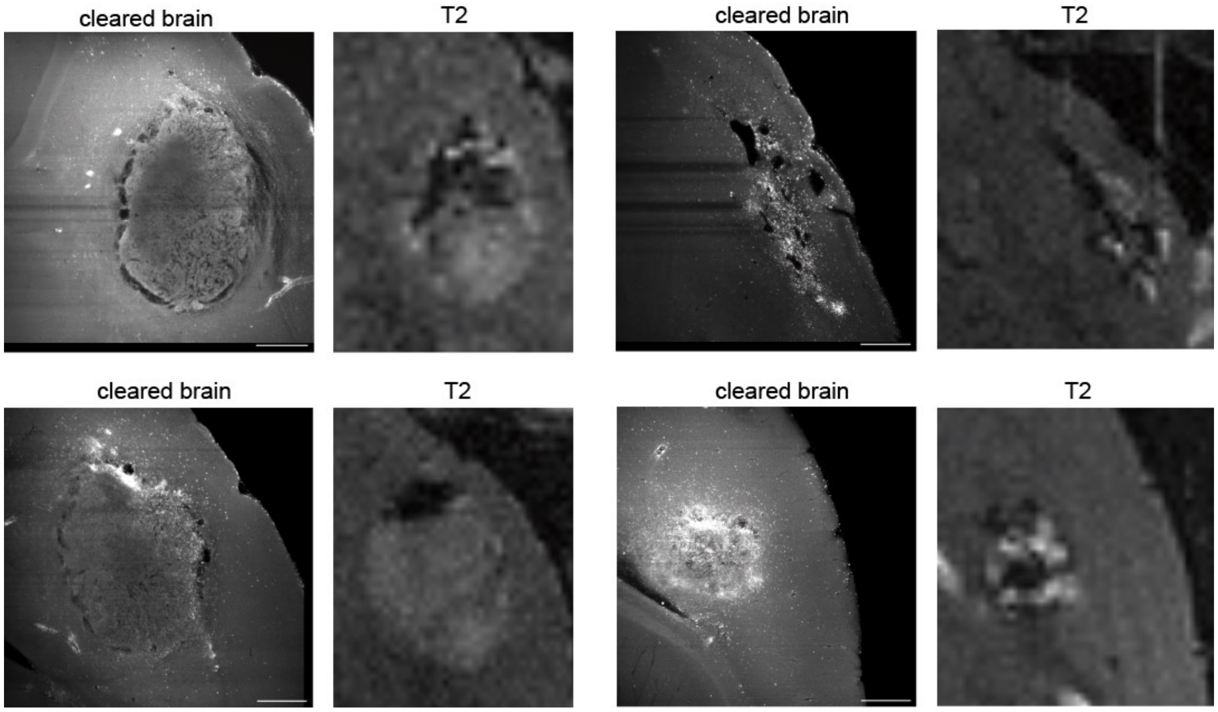

Figure 10: $CD3^+$ staining of cleared brains correlates with areas of reduced relaxation time by MRI

Iron oxide NP labeled T cells were injected intratumorally in a Gl261 model, brains were cleared with iDisco on d14 after ACT and stained for $CD3^+$. Images show cleared brains imaged by light sheet microscopy next to respective T2-weighted images by MRI; light sheet microscopy was supported by Berin Boztepe

Tracking of CAR T cells

Since personalized CAR T cell therapies are likely the future of cancer therapies, the goal was to extend non-invasive tracking of T cells to CAR T cells in a murine glioma model. CD70 specific CAR T cells were used for this purpose that can be utilized in the Gl261 tumor model after lentiviral overexpression of CD70 in the Gl261 cells. CAR T cells contained either a CD28 or 4-1BB costimulatory domain as well as the CD27 recognition domain. *In vitro* labeling with the iron oxide NP showed a labeling efficiency with a mean of 84.7% (figure 11C). Human CD19 CAR T cells could be labeled with iron oxide NP with high efficiency of 99.8% (figure 11D). Therefore, labeling with iron oxide NP is feasible not only in primary murine T cells, but also in murine as well as human CAR T cells. NP labeled human CD19 CAR T cells were co-incubated with NALM6 target cells and tested for their antigen-specific killing capacity. Non-transduced human T cells were used as control for the specificity of the target cell killing. While NP labeled CD19 CAR T cells killed the majority of target cells with 6-16% of target cells remaining, unlabeled CD19 CAR T cells killed more efficiently with only 1.14% remaining (figure 11E). Therefore, NP labeling slightly reduced CAR T cell killing activity, but the NP labeled CAR T cells were still able to perform efficient target cell killing.

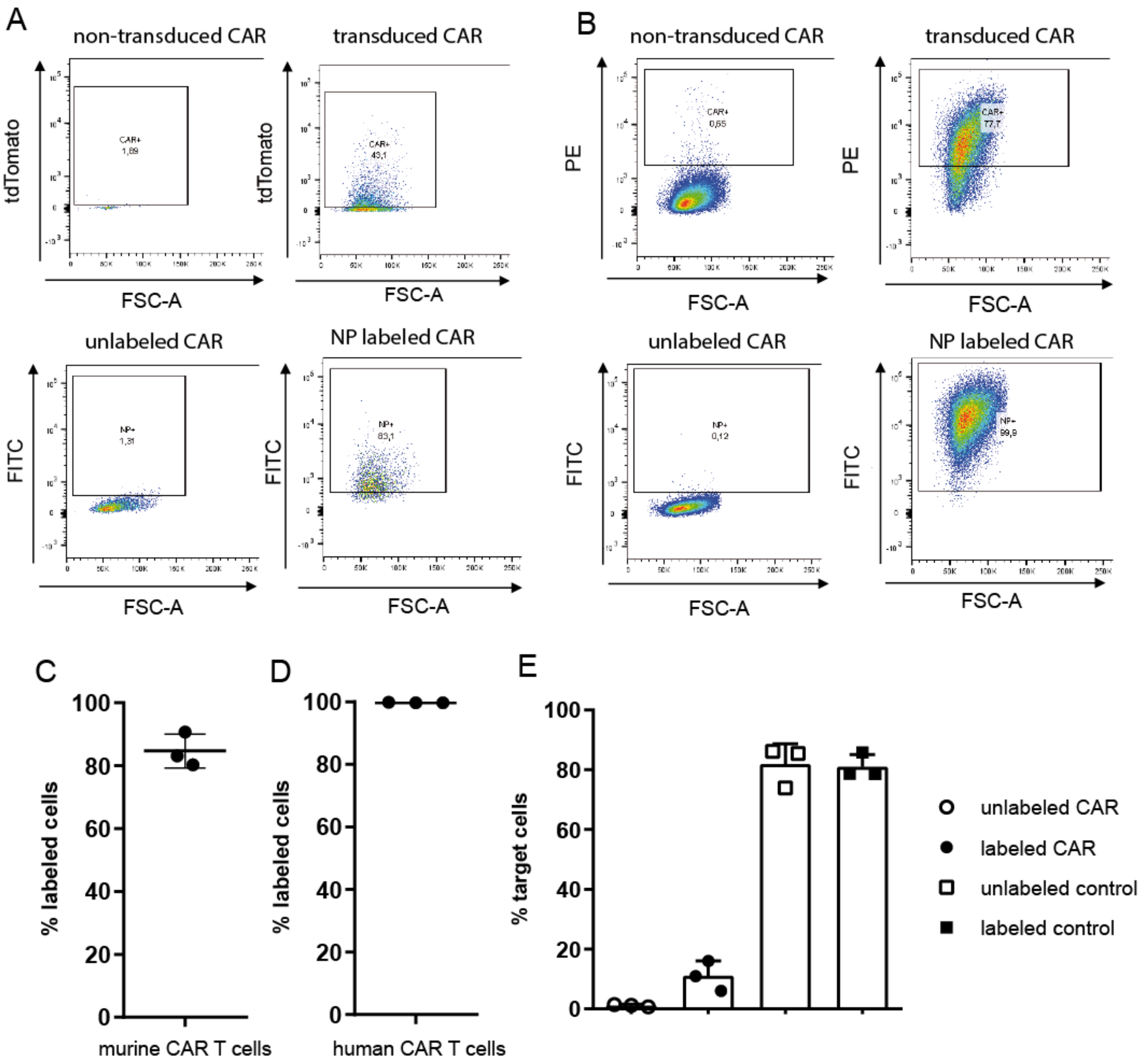

Figure 11: CAR T cells can be labeled with iron oxide NP

A NP labeling of murine CD70 CAR T cells, flow cytometry plots **B** NP labeling of human CD19 CAR T cells, flow cytometry plots **C** labeling efficiency of murine CD70 CAR T cells with iron oxide NP after 24 h, assessed by flow cytometry, displayed as mean + SD **D** labeling efficiency of human CD19 CAR T cells with iron oxide NP after 24 h, assessed by flow cytometry, displayed as mean + SD **E** killing activity of unlabeled vs. NP labeled human CD19 CAR T cells of NALM6 target cells in comparison to human T cells, assessed via counting beads by flow cytometry, displayed as mean ± SD

Alternative methods for T cell tracking

While non-invasive tracking by MRI could be an easily clinically translatable approach, PET has been proposed as a more sensitive method for cell tracking inlcuding T cell imaging. In addition, it could serve as a confirmation to data that have been obtained by MRI in this project.

As an initial experiment, T cells were tracked using a γ-imager, which can detect gamma radiation emitting radioisotopes. Primary murine T cells were incubated with indium-111 *in vitro* and adoptively transferred via i.v. injection in mice with a Gl261 tumor. In this case, indium-111 is taken up unspecifically by primary T cells. Mice were analyzed in a whole body γ-imager that detects the radioactive decay of indium-111 after 10 min, 30 min, 1 h, 2 h, 4 h, 24 h and 4 days (figure 12A) and organs were harvested for post-mortem analysis in a γ-counter (figure 12B). The γ-imager showed the highest signal in the spleen and liver of the mice. In accordance with this, post-mortem analysis using a γ-counter revealed the highest cpm/g in the liver, spleen and kidneys. The signal detected by the γ-counter was higher in the tumor than in surrounding brain tissue, which shows specific T cell infiltration of the tumor, albeit not detectable by γ-imager (figure 12C). Therefore, indium-111 labeled T cells could be visualized by γ-imager after intravenous ACT in the liver, spleen and kidneys, however the γ-imager sensitivity was likely not high enough for the low T cell infiltration of the brain and tumor. I therefore employed a non-invasive imaging method that would enable specific uptake of a radiotracer by the T cells to increase detection sensitivity: the expression of the somatostatin receptor 2 (SSTR2) in adoptively transferred T cells in combination with the radiotracer 177-Lu-DOTATOC or 68-Ga-DOTATATE could enable T cell tracking by PET. Both agents are similar to the endogenous hormone somatostatin and can bind to the SSTR2. They have a chelator site that is labeled with β+-emitting Ga-68 that can be utilized for diagnosis using PET or with β−-emitting radioisotopes such as Lu-177 for therapeutic purposes.[46] This method of expressing SSTR2 in T cells has previously been used by Vedvyas et al. in an anaplastic thyroid tumor model.[47] In contrast to MRI, PET has a higher sensitivity and the constant expression of SSTR2 mitigates the risk of possible tracer/NP dilution that could occur in MRI tracking approaches due to T cell proliferation. In addition, a stable expression of SSTR2 would enable repetitive long-term tracking of T cells, since multiple rounds of radiotracer injections could be performed. Human T cells were transfected with SSTR2 using a scaffold/matrix attachment region (S/MAR) approach and functionality of SSTR2-transfected T cells was confirmed in comparison with non-transfected T cells analyzing antigen-specific killing activity. S/MAR is a non-viral genome editing method that is based on episomes and enables persistent transgene expression.[48] SSTR2-transfected human T cells were incubated with the radiotracer DOTATOC and radiotracer uptake of the T cells was assessed using a γ-counter after 1 h (figure 12D). Human T cells were used due to the higher clinical relevance as well as the low transfection efficiency of SSTR2 with murine T cells. DOTATOC was taken up specifically by SSTR2-transfected T cells compared to mock-transfected T cells. This was further confirmed by incubation with the inhibitor ocreotide, which led to no DOTATOC uptake when incubated simultaneously in SSTR2-transfected T cells (figure 12D). In addition to primary T cells, Jurkat cells (J76) were transfected with SSTR2 and tested for DOTATOC uptake. With a mean of 4139 cpm, radiotracer uptake was almost doubled in Jurkat cells compared to primary T cells with an average uptake of 2311 cpm. Ocreotide addition to this sample resulted in no radiotracer uptake as well (figure 12D). AR42J cells were used as positive control, since this is a SSTR2 positive pancreatic tumor cell line.[49] However, uptake of DOTATOC was almost 50 times higher in AR42J cells than in SSTR2-transfected human primary T cells (figure

12D). Despite of the radiotracer uptake in SSTR2-transfected T cells being significantly higher than in mock-transfected T cells – which shows that the DOTATOC uptake is indeed specific – uptake was too low and remained below PET detection limit. Even after increasing SSTR2 expression levels by increased DNA usage, uptake remained comparatively low, which is why further optimization of the radiotracer uptake remains to be done in a future study before PET imaging can be performed.

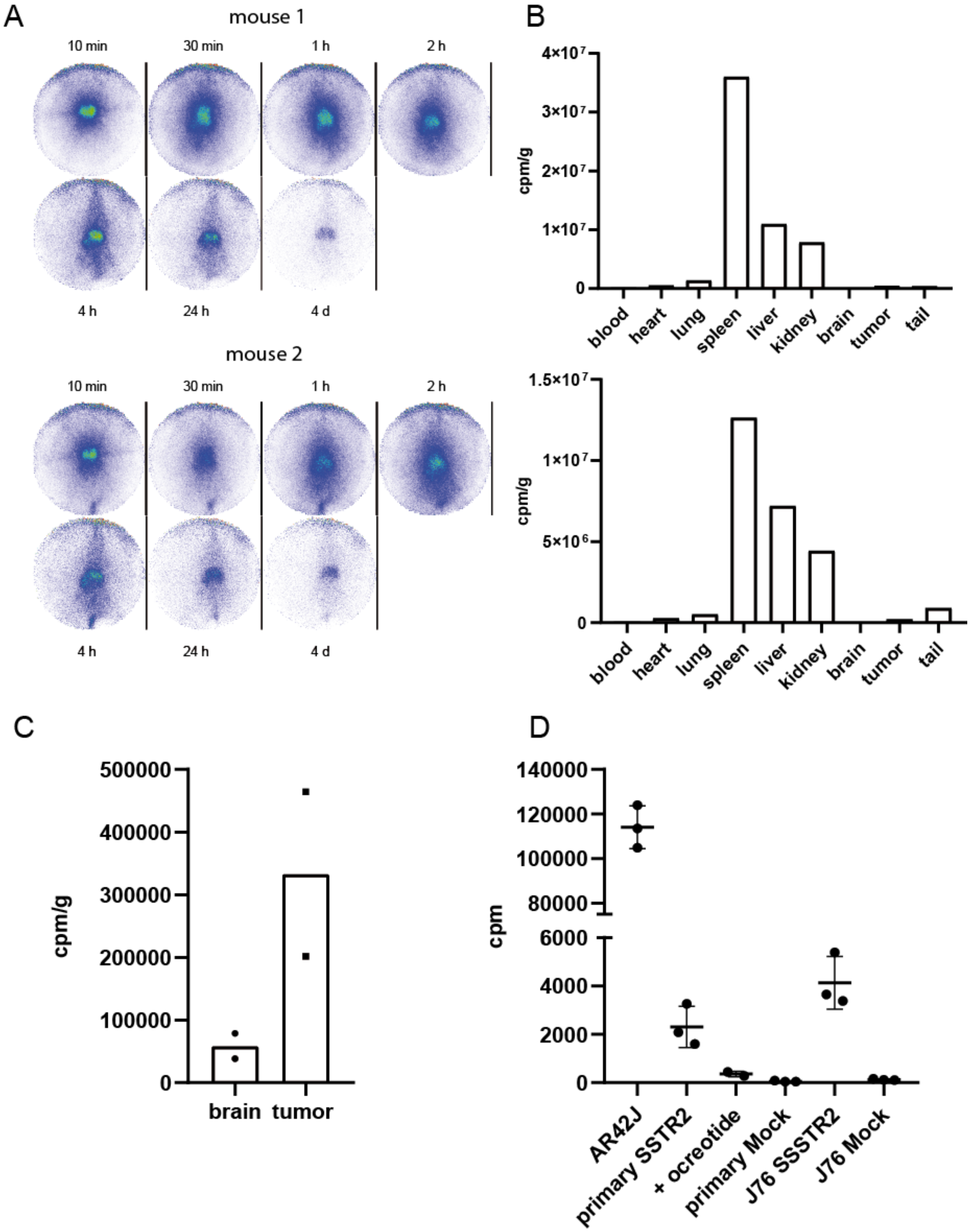

Figure 12: T cells can be tracked non-invasively by γ-imager

A Distribution of indium labeled murine T cells 10 min, 30 min, 1 h, 2 h, 4 h, 24 h and 4 d after ACT by γ-imager **B** Quantification of cpm/g per organ 4 d after ACT by γ-counter **C** Comparison of cpm/g of tumor vs. surrounding brain tissue 4 d after indium labeled ACT by γ-counter **D** Uptake of 177-Lu-DOTATOC of AR42J cells vs. primary human T cells transfected with SSTR2 vs. human primary T cells vs. J76 cells transfected with SSTR2 vs. J76 cells after 1 h of incubation, displayed as mean ± SD

Discussion

Malignant gliomas have a poor response to immunotherapy and survival rates have remained stagnant in the past years.[1] Intratumoral T cell homing and activity can currently only be assessed based on biopsies; however repeated biopsies are not practical and represent a high burden for patients. Therefore, a non-invasive method enabling the tracking of immune cells is needed in order to assess biodistribution of T cells and monitor therapy efficiency. A large proportion of iron oxide NP based cell tracking has previously focused on stem cells due to their ability to take up large amounts of NP, however a study on NP labeled T cell tracking *in vivo* had not been performed to this extent, especially not in gliomas.[50–52] In this study I show that non-invasive visualization of T cells in a murine glioma model by MRI using iron oxide NP is possible.

The T cell labeling approach used in this study does not require additional devices or methods such as electroporation, but is based on T cell activation by IL-2, which is a clear advantage compared to other labeling approaches. Kiru et al. have employed a microfluidics device for cell volume exchange for convective transfer in their iron oxide NP labeling approach of T cells.[44] Thu et al. have used a T cell labeling approach with the iron oxide NP ferumoxytol (FeOx) that requires incubation with heparin and protamine, which leads to the formation of nanocomplexes.[43] FeOx does not have a fluorescent conjugate; in contrast, with the NP used in my study, intracellular labeling can be confirmed by flow cytometry as well as confocal microscopy based on the fluorescent FITC conjugate, which is an advantage. I could show that primary murine T cells can be labeled with the iron oxide NP very effectively, reaching ~100% labeling efficacy *in vitro*, and that additionally murine as well as human CAR T cells can be labeled with the NP. I could provide evidence that iron oxide NP labeling does not affect

T cell viability or cytokine secretion *in vitro*. T cell viability generally quickly decreased *in vitro* also in the unlabeled condition when comparing the viability after 24 h of culturing to 48 h, which should be improved in follow up studies and could likely be solved by an adjustment of medium components. However, this effect was observed in the unlabeled as well as in the labeled condition and T cells maintained their antigen-specific killing activity *in vitro* as well as *in vivo*. TEM showed that NP are located within intracellular vesicles, which suggests an endocytic uptake mechanism. However, the detailed uptake mechanism of the NP into T cells remains to be investigated. Charpentier et al. showed that T cells are capable of macropinocytosis – a type of endocytosis in which the cell membrane ruffles in order to take up large amounts of extracellular fluid, macromolecules and metabolites.[53] Macropinocytosis has been suggested as an uptake mechanism of NP in other immune cell types[54], therefore it is likely that iron oxide NP are also taken up by T cells via macropinocytosis.

Despite of the LDH release assay showing slightly reduced antigen-specific killing activity after NP labeling, I believe that due to the RTCA showing no difference in tumor cell eradication that T cells are still able to fulfill their function after NP labeling. NP labeled human CD19 CAR T cells showed a reduced cytotoxic activity compared to unlabeled CD19 CAR T cells, however, they were still able to efficiently kill around 90% of target cells. In a therapeutic setting, NP labeling would therefore possibly require the use of an increased amount of CAR T cells compared to unlabeled CAR T cells to ensure tumor eradication. Furthermore, analysis of T cell exhaustion markers of NP labeled T cells after ACT showed that labeled T cells are not more exhausted than unlabeled T cells *in vivo* and tumor eradication after ACT with NP labeled T cells could still take place up to complete tumor response.

ICP-OES showed that with the incubation of NP containing 50 μg Fe/1x10^6 T cells, an intracellular iron concentration of 2 pg Fe/cell can be achieved. Maximal iron concentration per cell that I observed was 3.2 pg Fe/cell. Due to the saturation, an increased addition of NP would only lead to minorly increased intracellular iron concentration, while potentially influencing T cell function. Kiru et al., who used FeOx, demonstrated an average iron uptake of 1.19 pg/cell.[44] By using ferucarbotran, Rivera-Rodriguez et al. achieved an uptake of 0.4 – 1 pg Fe/cell.[55] Compared to these studies, I could achieve a roughly doubled uptake of iron per cell with the Molday ION BioPAL NP. Macrophages took up around 2 pg Fe/cell as well when incubated with the same NP concentration. It has been reported that by using a magnetothermal labeling approach, mesenchymal stem cells could be loaded with up to 150 pg Fe/cell.[56] However, it is unlikely that T cells, which have only a small cytoplasm in comparison, could be labeled with these high amounts of iron. Iron concentration per cell likely directly relates to detection sensitivity by MRI, in addition to MRI field strength. Using iron oxide NP labeling, single cell tracking of T cells is not possible. However, assessment of sensitivity in a healthy mouse brain showed that as few as 10,000 Molday ION BioPAL NP labeled T cells are sufficient to significantly reduce the relaxation time compared to unlabeled T cells. Kiru et al., who used FeOx as CAR T cell labeling agent in an osteosarcoma model, have described a detection limit of 20,000 cells *in vitro*.[44] The labeling approach with Molday ION BioPAL used in my study with a detection limit of 10,000 T cells *in vivo* is therefore more sensitive than their approach. Masthoff et al. describe a tracking approach of single monocytes intracranially using Ferucarbotran in a time-lapse MRI manner.[57] However, the authors could not rule out that their approach tracked cell clusters and not single cells. Furthermore, there was no quantification of the amount of iron on a single monocyte level. A higher iron concentration of the NP could further increase detection sensitivity, would however require additional tests regarding NP toxicity. Since ICP-OES showed that in my experimental approach T cells were labeled with 2 pg Fe/cell and that NP uptake is almost saturated at that point, iron concentration of the NP itself should be increased rather than increasing the amount of NP added to the T cell cultures. This might however influence NP size and consequently affect the intracellular uptake. Sensitivity is further influenced by gradient strength of the instrumentation used and could possibly be decreased in clinical 3 Tesla scanners compared to the 9.4 Tesla small animal MRI used in this study, which should be considered when translating the non-invasive tracking approach to the clinical setting. Once the uptake mechanism is understood in molecular detail, the uptake pathway could possibly be hijacked so that an increased amount of NP could be taken up per T cell, which would likely increase detection sensitivity by MRI.

NP labeled T cells are still detectable after 14 days, which shows that long-term tracking of T cells and therefore long-term treatment monitoring without the need for additional injections is possible. The maximum detection period of NP labeled T cells is not known and likely depends on proliferation of the T cells. An ideal immune cell tracking method should have a low background and furthermore be non-immunogenic. With the use of iron oxide NP labeled T cells, there is low background since the brain tissue and tumor have a significantly higher T2* relaxation time than the NP labeled T cells. Blood contains iron due to the hemoglobin and an intracranial bleeding could therefore also reduce relaxation time and interfere with data interpretation; especially the intratumoral delivery route could cause microbleedings. However, I did not observe any areas with reduced relaxation time in the group of mice that had received unlabeled T cells intratumorally, which does not exclude the possibility of bleedings in the group that received labeled T cells, but provides evidence that the detectable signal is very likely based on the labeled T cells and not on intratumoral bleedings. In addition, immunohistochemistry showed a correlation of adoptively transferred T cell location with iron accumulation at the same spots as areas of reduced relaxation time detected by MRI. Correlation of areas of reduced relaxation time and T cell location was further validated by whole brain clearing and light sheet microscopy, which confirmed an overlap of the respective signals. Therefore, the signal detected by MRI is very likely based on the intracellular iron oxide NP and allows tracking of adoptively transferred T cells.

I could show that a low mean relaxation time of the tumor area at an early time point (d3 after intratumoral ACT with NP labeled T cells) correlates with partial or complete tumor response, while a high mean relaxation time of the tumor area at an early time point leads to progressive or stable disease. A decreased mean relaxation time of the tumor area means that T cells have likely redistributed within a majority of the tumor. In contrast, a high mean relaxation time means that T cells have accumulated locally – mostly on the tumor border – and not distributed within the tumor as also visible by eye on MR images (figure 9). A greater distribution of T cells could therefore indicate an increased anti-tumor activity, especially in the tumor core. Reproducibility of these results was achieved in a second, independent experiment. Underlying mechanisms and reasons for uneven distribution of T cells between animals are unclear and remain to be investigated. T cell exhaustion and tumor heterogeneity could have an effect on the observed divergent T cell distribution. The study on NP labeled CAR T cells in an osteosarcoma model by Kiru et al. confirms that T2* relaxation times of the tumor at an early time point after ACT can function as a predictive biomarker for tumor response in a similar fashion to what I have observed in this study.[44]

I have performed non-invasive visualization of T cells and correlation of response or resistance with relaxation times after intracranial T cell injections. Even though there are local, intratumoral delivery approaches for cytokines[58] and there are reports of CAR T cell infusions into the resected tumor cavity, antigen-specific T cells in patients within clinical trials are usually delivered via intravenous injections. Ideally, T cell tracking would therefore be performed after i.v. ACT due to its clinical relevance. When performing non-invasive T cell tracking after i.v. injections, whole body tracking could be employed to understand infiltration routes and monitor possible off-target effects.[59] However, I could not perform T cell tracking after i.v. injections, since several independent experiments have shown that the Gl261-GP100 model is not suitable for that, because only a minor proportion of the adoptively transferred T cells are recruited to the TME, which is likely due to the weak antigen and active tumor immune escape. The blood brain barrier (BBB) might contribute to the low T cell recruitment to the tumor after i.v. ACT. Irradiation of mice with 2 x 2 Gy did not improve recruitment of adoptively transferred T cells, despite of reports that low dose irradiation increases T cell recruitment to the tumor.[32] Gl261-Ova in contrast seemed to be too immunogenic for this approach with cases of tumor regression after PBS injection that are likely based on the endogenous T cells. The role of the endogenous T cells can however not be visualized by MRI in this approach. Gl261-SIINFEKL, which only contains the Ova epitope could possibly be used in follow up studies for non-invasive T cell tracking. Intraventricular ACT is another alternative injection route, which I have used in the Gl261-GP100 model. However, after 4 days, NP labeled T cells were not detectable intratumorally by MRI and stainings on cryoslides showed no infiltration of the tumor by PMEL T cells. In order to further establish non-invasive T cell tracking, a suitable mouse model with sufficient T cell infiltration of the tumor would be needed. Schaettler et al. have seen a survival benefit, but also heterogenous response after ACT with a

TCR specific for the Imp3D81N neoantigen that was identified in the Gl261 model.[60] They partly attributed the fact that a proportion of mice still succumbed to the tumor to increased T cell exhaustion and antigen heterogeneity within the tumor, but infiltration of adoptively transferred T cells was not further quantified and recruitment of T cells to the TME was not visualized non-invasively. Their model could potentially be used for non-invasive T cell tracking using iron oxide NP.

Iron oxide NP labeling enables the tracking of T cell location and distribution, however it does not provide any information about T cell exhaustion state or antigen specificity. There is furthermore the possibility of tracking exhausted T cells since viability and functional status cannot be assessed by non-invasive tracking by MRI. Another limitation of this approach is that T cells have to be labeled *ex vivo* and that therefore only adoptively transferred cells can be tracked by MRI, neglecting the role of endogenous T cells. *Ex vivo* labeling of T cells was chosen, since it is known that FeOx is taken up by astrocytes and macrophages *in vivo*, which is why it is very likely that the NP Molday ION Biopal used in this study would also be taken up by other immune cells and could consequently not be differentiated by MRI.[61] A direct i.v. application of the NP would therefore likely not lead to specific tracking of T cells.

Even though the lack of information on the biodistribution of the T cells in patients has been described as key limitation for the advancement of T-cell therapy,[44] intratumoral T cell distribution is however not the only factor influencing the efficacy of immunotherapy. T cell activity and binding affinity of a TCR to an antigen does not automatically correlate with T cell activation in response to antigen presentation on cells.[62] Chen et al. could additionally show that interaction of T cells with microglia plays a major role in anti-tumor effects.[63] Furthermore, ICB response is influenced by the interaction with dendritic cells[64,65] and also by interaction with B cells.[66] In an optimal tracking approach, T cell visualization would therefore also account for interaction with other immune cells in the TME. Visualizing cell-cell interactions by MRI is however currently not possible. The observed differences in T cell distribution between animals could possibly be explained by T cell activity/exhaustion, interaction with other immune cells and areas of hypoxia or tumor heterogeneity.[67]

In my approach I have focused on CD8+ T cells, since they are the cytotoxic T cells eliciting an anti-tumor effect via interaction with APCs, however, several studies such as Alspach et al. have provided evidence for a leading role of CD4+ T cells in cancer immunosurveillance.[63,68,69] T cell tracking by MRI using iron oxide NP could easily be transferred to CD4+ T cells as well.

The use of iron oxide NP is limited to tracking only one cell population at a time. However, there are approaches to combine iron oxide based tracking with gadolinium (Gd) based cell tracking in a dual color tracking approach.[70] While iron oxide NP labeled cells are visualized in a T2* sequence, Gd labeled cells can be detected using a T1-weighted sequence in this setup. Concentrations of both agents have to be carefully assessed in order to achieve T1 enhancement without influencing T2-weighted images. Loai et al. have managed to combine Gd_2O_3 -labeling and SPIO-labeling and visualize two different cell populations at the same location *in vitro*.[70] This technique could enable to monitor for example adoptively transferred $CD8^+$ T cells and adoptively transferred $CD4^+$ T cells simultaneously and differentiate between the two populations. Alternatively, adoptively transferred T cells injected at two different locations could be tracked in a pre-clinical setting to follow infiltration routes.

Due to their phagocytotic abilities, macrophages might be able to take up iron oxide NP to some extent *in vivo*.[71] While ACT of macrophages is not commonly used as a treatment approach, the role of macrophages in cancer immunosurveillance could be understood more deeply using non-invasive tracking.[72] Therapy against CD47, which is overexpressed on certain tumor cells and binds to signal regulatory protein α (SIRPα) inhibiting phagocytosis by macrophages via a so called “don’t eat me”-signal, could potentially be monitored in glioma as it has already been successfully shown in a preclinical osteosarcoma model.[73,74] However, when tracking macrophages, a differentiation between pro- and anti-inflammatory macrophages would be essential in order to understand and predict their role in the TME, which can hardly be achieved with iron oxide NP.

Another novel technique for the detection of SPIOs is magnetic particle imaging (MPI). Rivera-Rodriguez et al. tracked ferucarbotran labeled T cells by MPI. [55] Since they observed a decreased iron uptake per cell with 0.4 to 1 pg Fe/cell compared to 2 pg/cell that was achieved with Molday ION BioPAL, the detection limit was therefore only at 5×10^4 cells. Even though the authors were able to detect iron oxide NP labeled T cells in a glioblastoma model, they did not correlate infiltration or intratumoral distribution with tumor response. MPI requires coregistration with other imaging modalities for anatomical reference, since it can only detect signal from the superparamagnetic iron oxide NP itself.

However, magnetic based imaging is not the only non-invasive approach that can be used to monitor immune cells. I utilized indium-111 and a γ-counter as well as γ-imager for the detection of primary murine T cells. After i.v. injection of indium-111 labeled antigen-specific T cells, the majority of signal was detectable in spleen, liver and kidneys by γ-imager, which correlated with the highest cpm/g counts detected in the respective organs by the γ-counter post-mortem. While the tumor contained more cpm/g than the surrounding healthy brain tissue, the signal detected in tumor tissue by the γ-counter was still comparatively extremely low, which indicates that only a minority of antigen-specific T cells migrated to the brain and infiltrated the tumor. This observation could again be attributed to issues with the Gl261-GP100 model already observed by MR imaging. Therefore, it is not surprising that there was no T cell-specific signal detectable in the brain by γ-imager, but only in the spleen and liver. Hence, non-invasive imaging of T cells is possible by γ-imager in a pre-clinical setting, however, this approach was not suitable for the Gl261-GP100 model with its low amount of T cell infiltration in the brain.

T cell tracking by CT could furthermore function as an alternative method to MRI approaches. Meir et al have tracked T cells labeled with gold nanoparticles by CT in a melanoma model.[75] The combination of CT with PET (PET/CT) could further increase sensitivity for cell visualization. Therefore, while MRI has the advantage of being radiation-free, the combination of PET and CT results in a higher sensitivity for cell visualization than MRI. In an approach previously described by Vedvyas et al., T cells were transfected with SSTR2,[47] which has the advantage that no dilution takes place as it could happen with iron oxide NP labeling during proliferation. However, in contrast to NP based tracking, this approach requires genetic modification of the T cells. There is a limited basal expression of SSTR2 throughout the body, which limits background activity. In addition, only live cells are able to express the transfected reporter; therefore, no imaging of dead cells would take place. However, in contrast to MRI, PET requires the use of radiotracers that have to be injected intravenously before every imaging. I could show that SSTR2-expressing T cells specifically take up the radiotracer DOTATOC compared to mock-transfected T cells, which was furthermore confirmed by a control condition with the inhibitor ocreotide. However, radiotracer uptake was 50 times higher in SSTR2-expressing AR42J cells. Conditions with J76 cells showed that the low radiotracer uptake is not only an issue in primary T cells, but also in the Jurkat cell line. Low radiotracer uptake might be caused by mechanisms inherent to T cells such as immediate ejection of the NP and very limited cytoplasm space. Alternatively, the SSTR2 construct I was using might have been malfunctioning or suboptimal. Despite of extensive trouble shooting, DOTATOC uptake in SSTR2-expressing T cells was therefore not high enough for PET imaging in my experiments.

Nagle et al. have used radiolabeled CD8$^+$ mini-bodies to track T cell recruitment to the TME by PET/CT in a humanized mouse model.[76] CD8$^+$ minibodies are novel engineered antibody fragments. In addition to CD8$^+$ T cells, Nagle et al. also managed to visualize CD4$^+$ T cells non-invasively using immunoPET.[77] In this approach, not only adoptively transferred T cells, but also endogenous T cells can be tracked, which is a clear advantage and could provide a deeper understanding of ongoing immunogenic processes. However, antigen-specific T cells cannot be differentiated from unspecific T cells and exhausted T cells can also not be detected with this approach. Woodham et al were able to detect antigen-specific CD8+ T cells *in vivo* by dimeric major histocompatibility molecule scaffolds called synTac using immunoPET.[78] This approach accounts for TCR specificity. CD8+ mini-bodies seem to be a more promising approach for T cell tracking by PET/CT and should possibly rather be followed up than the SSTR2 approach, which requires genetic engineering of T cells. Shin et al. have developed a SyNthetic Intramembrane Proteolysis Receptor (SNIPR) reporter system that enables tracking of epidermal growth factor receptor variant III (EGFRvIII) specific T cells by PET and therefore represents another promising approach for the tracking of antigen-specific T cells.[79]

While these PET/CT based approaches are not tested in clinical trials yet, the iron oxide NP FeOx, which was originally approved for treatment of iron deficiency in chronic kidney disease, is already used in an off-label approach in the clinic for example within the scope of imaging of the CNS.[80,81] FeOx is described as well tolerated with few adverse effects in the context of MRI.[82] The use of other iron oxide NP for T cell labeling in order to differentiate between response and resistance at an early time point should therefore be easily transferable to clinical use. However, further optimization would be needed when translating this approach from the 9.4 Tesla small animal MRI used in this study to clinical MRI, which commonly has a field strength of 3 Tesla. Since it is expectable that initial/baseline relaxation time varies from patient to patient as observed in mice in this study, relative relaxation time based on an MRI before ACT should be used in order to monitor the ACT. Despite of multiple required MRIs, non-invasive treatment monitoring has the advantage that it does not add any additional burden to the patient, who usually undergoes MRI for tumor monitoring anyway. The tracking of T cells by iron oxide NPs could not only allow the monitoring of treatment effects, but also enable the tracking of off-target effects and therefore provide a valuable tool monitoring new immunotherapeutic approaches and patients' health. Furthermore, immune cell tracking could be complemented with chemical exchange saturation transfer (CEST) – used to visualize metabolites – or elastography, which assesses the stiffness of the tumor. CEST and elastography have the advantage that they do not require any imaging agents. Both approaches are already tested in a clinical setting and could provide additional information about immune cell recruitment and intratumoral distribution.[83–85] In addition to glioma, other solid cancer entities such as gastric cancer could also benefit from non-invasive tracking, especially during immunotherapy.[86] Additional fields for NP-based tracking of T cells could be envisioned for treatment monitoring of autoimmune diseases such as multiple sclerosis (MS)[87] or or other neuroinflammatory conditions mediated by T cell immunity such as Lewy body dementia.[88]

Conclusion

In conclusion, T cells can be successfully labeled with iron oxide NPs without affecting their viability or effector functions. T cells can be visualized intratumorally in a murine glioma model non-invasively by MRI over a time period of at least two weeks and immunohistochemistry as well as light sheet microscopy have confirmed that the detected signal is based on intracellular iron in the adoptively transferred T cells. Furthermore, I could show that a low mean relaxation time of the tumor at an early time point correlates with partial or complete tumor response and that non-invasive T cell tracking therefore has the potential to predict tumor response and resistance.

Material and Methods

List of Materials

Antibodies used for IHC

Antibody	Company	Order number
CD90.1 APC	BioLegend	202526
CD3	Dako	A0452
Alexa-546nm secondary AB	ThermoFisher	A11010
Vectashield DAPI antifade mounting medium	Biozol	H-1200
Eukitt mounting medium	Sigma Aldrich	30989

Table 1: Antibodies used for IHC

Antibodies used for flow cytometry

Antibody	Company	Order number
fixable viability stain eFluor 780	BD Horizon	565388
CD3 murine BV510	BioLegend	100233
CD8 AF700	BioLegend	100730
CD45.1 PE-Cy7	BioLegend	110730
CD45.2 APC	BioLegend	109814
CD90.1 PE-Cy7	BioLegend	202517
CD11b BV711	BioLegend	101241
PD-1 PerCP-eFl710	ThermoFisher	46-9985-82
Lag3 BV785	BioLegend	125219
Tim3 BV421	BioLegend	119723
CD3 human PE	BioLegend	300308
CD19 BV510	BioLegend	363020
R-Phycoerythrin AffiniPure F(ab')$_2$ Fragment Goat Anti-Human IgG (H+L)	Jackson ImmunoResearch	109-116-088
anti-CD16/CD32	eBioscience	93 14-0161
Counting beads	Invitrogen	01-1234-42

Table 2: Antibodies used for flow cytometry

Antibodies used for clearing/light sheet microscopy

Antibody	Company	Order number
CD3	Dako	A0452

Table 3: Antibodies used for clearing

Cell culture media

Medium	Company	Order number
DMEM	Sigma-Aldrich	D6429

FBS Superior	Sigma Aldrich	S0615
Penicilin/Streptavidin	Sigma Aldrich	P4333
Trypsin-EDTA	Gibco	25300-054
Accutase	Sigma Aldrich	A6964-100
PBS	Capricorn	PBS-1A
RPMI-1640	PAN-Biotech	P04-18500
F-12K	ThermoFisher	21127022
Clicks medium	Sigma Aldrich	C5572
b-Mercaptoethanol	Sigma Aldrich	M3148
L-Glutamine	Safc	59202C
HEPES	Sigma Aldrich	H0887
Sodium Pyruvate solution	Gibco	11360-070
Non-essential amino acids	Sigma Aldrich	M7145
Blasticidin	Gibco	A11139-03
Recombinant human IL-2	PeproTech	200-02
Recombinant human IL-7	PeproTech	200-07
Recombinant human IL-15	PeproTech	200-15
CD3e monoclonal antibody	ThermoFisher	14-0031-85
Anti-mouse CD28	BioLegend	BLD-102102
ACK lysis buffer	Gibco	A10492-01
Hank Balanced Salt Medium	Sigma Aldrich	H9269

Table 4: Cell culture media

Material

Material	**Company**	**Order number**
T175 cell culture flask	Greiner	660160
96 well U bottom plate	TPP	92097
6 well suspension plate	Sarstedt	83.3920.500
LS columns	Miltenyi Biotec	130-042-401
Superfrost glass slide	ThermoFisher	J1800AMNZ
70 µm cell strainer	Greiner	542070
100 µm cell strainer	Greiner	542000
RTCA ePlates	Agilent	300601010

Table 5: Material

Kits

Kit	**Company**	**Order number**
CD8+ T cell isolation kit	Miltenyi Biotec	130-104-075
LDH release assay	Cell Signaling	37291
eBioscience Intracellular Fixation & Permeabilization Buffer Set	invitrogen	88-8824-00
Prussian blue staining kit	BioPAL	CL-01-50

Table 6: Kits

Chemicals and reagents

Chemical/reagent	**Company**	**Order number**
Molday ION EverGreen	BioPAL	CL-50Q02-6A-51

Percoll	Cytiva	17089101
haematoxylin	Sigma Aldrich	MHS32
eosin	Sigma Aldrich	318906
methanol	Sigma Aldrich	32213
ethanol	Supelco	1009832511
4.5% Formaldehyde ROTI Histofix	Carl Roth	2213.5
acetone	VWR chemicals	2006330
pararosalinine	Sigma Aldrich	HT203
Hydrogen peroxide suprapur	Supelco	1072980250
Xylole	Roth	97135
Nitric acid	Honeywell	30-709
TWEEN	Sigma Aldrich	P4780-500
TissueTek	Sakura	4583
Ionomycin	Sigma Aldrich	I0634
PMA	Sigma Aldrich	P8139
Brefeldin A	Invitrogen	00-4506-51
DMSO	Roth	4720.1
Albumin Fraction V	Roth	01634
EDTA	ThermoFisher	J62948.A1
Liberase D	Roche	5466202001
normal goat serum	Sigma Aldrich	G6767
25% EM-grade glutaraldehyde	Electron Microscopy Sciences	16200
16% EM-grade paraformaldehyde	Electron Microscopy Sciences	15710

Table 7: Chemicals and reagents

List of equipment

Equipment	**Company**
Cryotome CM1950	Leica
Axio scan.Z1	Zeiss
UltraMicroscope II	Miltenyi
9.4 Tesla MRI scanner	Bruker
LSM 700 confocal microscope	Zeiss
FACS Canto II Analyser	BD Biosciences
LSR Fortessa HTS Analyser	BD Biosciences
Stereotact	Stoelting
Drill	Stoelting
701 Syringe 10 µl #80308	Hamilton
Incubator MCO-18AIC	Sanyo
xCelligence RTCA reader	Agilent
iMark microplate absorbance reader	BioRad
ICP-OES 720	Agilent
Transmission electron microscope	JEOL JEM 2100 Plus
γ-imager	Perkin Elmer
γ-counter	Perkin Elmer

Table 8: Equipment

Mice

Specific and Opportunistic Pathogen Free (SOPF) female C57Bl/6J mice were purchased from Janvier Laboratories at the age of 6-10 weeks. All animal protocols were performed in compliance with the laboratory animal research guidelines and were approved by the governmental authorities (animal protocols: G27-17 and G35-22, regional administrative authority, Regierungspräsidium Karlsruhe, Germany). PMEL mice carry a rearranged T cell receptor transgene specific for the mouse homologue (pmel-17) of human silver locus protein homolog (SILV), gp100, and were used as donor mice for primary murine T cells. OT-1 mice carry a transgenic T cell receptor which was designed to recognize ovalbumin residues 257-264 in the context of H2Kb and were also used as donor mice for T cells.

Cell lines

Gl261 cells were purchased from the National Cancer Institute Tumor and cultured in Dulbecco's modified Eagle's medium (DMEM) supplemented with 10 % fetal bovine serum (FBS) and 100 U/ml penicillin and 100 µg/ml streptomycin (all Sigma-Aldrich) at 37°C, 5% CO2. Gl261 cells were routinely tested for contamination by multiplex cell contamination test (Multiplexion GmbH). Cells were stored frozen using a 1:9 mixture of DMSO and FBS in liquid nitrogen for long-term storage and thawed using pre-warmed cell culture medium. For passaging, cells were detached using trypsin-EDTA, stopped by cell culture medium. Passaging was performed twice per week in a 1:10 ratio and cells were not passaged more than ten times. Gl261-Ova cells were incubated with 2.5 µg/ml blasticidin for positive selection. Nalm6 cells were cultured in Clicks medium supplemented with 10% FBS.

Tumor cell inoculation

Cells were detached from the cell culture flask using accutase, stopped by PBS. 1 x 10^5 Gl261 tumor cells were diluted in 2 µl sterile PBS and stereotactically implanted into the right basal ganglia of 7-11 weeks old female C57Bl/6J mice (coordinates: 2 mm right lateral of the bregma and 1 mm anterior to the coronal suture with an injection depth of 3 mm below the dural surface) using a 10µl Hamilton micro-syringe driven by a fine step stereotactic device.

MR imaging

Multiparametric MR imaging was performed according to Turco et al.[36] on a 9.4 Tesla horizontal bore small animal NMR scanner (BioSpec 94/ 20 USR, Bruker BioSpin GmbH, Ettlingen, Germany) with a four-channel phased-array surface receiver coil. MR imaging included a standard RARE T2-w sequence to monitor tumor volume (T2-w parameters: 2D sequence, 0.078 mm in-plane resolution, TE: 33 ms, TR: 2500 ms, flip angle: 90˚, acquisition matrix: 200 x 150, number of averages: 2, slice thickness: 0.7 mm, duration: 2 min 53 s; T1-w parameters: 2D sequence, 0.1 mm in-plane resolution, TE: 6 ms, 1000 TR: ms, flip angle: 90˚, acquisition matrix: 256 x 256, number of averages: 2, slice thickness: 0.5 mm, duration: 5 min). Further functional MR imaging included multi-gradient echo imaging (MGE parameters: 3D sequence, 0.1 mm in-plane resolution, TE: 2.57 ms, TR: 73.43 ms, flip angle: 20°, acquisition matrix: 200 x 200, number of averages: 2, slice thickness: 0.1 mm, duration: 22 min 7 s). MGE imaging was used for T cell tracking using the iron oxide NP Biopal. Imaging was performed before and on several time points after ACT.

For MRI, animals were anesthetized with 3% isoflurane. Anesthesia was maintained with 1–1.5% isoflurane. Animals were kept on a heating pad to maintain constant body temperature, and respiration was monitored externally during imaging with a breathing surface pad controlled by a LabVIEW program developed in house (National Instruments Corporation).

Analysis of MRI data

MR images were exported as DICOM files and visualized in using open-source Slicer Software (3D Slicer V. 4.10.2, www.slicer.org). Tumor volume was segmented semi-automatically using Slicer's Segment Editor module. T2*-relaxation times were calculated from MGE raw data and exported as T2*-relaxation maps in DICOM-format using a customized script (MATLAB R2020a, 64-bit version for Windows, MathWorks). The customized MATLAB script was kindly provided by Volker Sturm. Mean T2*-relaxation time of the entire tumor volume in ms was extracted for further analyses. Subsequent MRI time points were coregistered using the Slicer elastix module.

Tumor response criteria

Tumor response criteria were based on weekly MR imaging. For tumor monitoring, MRI imaging was performed 2 weeks after tumor inocculation (baseline, day 13), followed by tumor monitoring on day 3, 7, 10 and 14 after intracranial T cell injection. Classification of tumor response was assessed according to Aslan et al., 2020, as the following: CR was defined as relative increase in lesion volume pre MRI – d14 (%VpreMRI–MRId14) of −100%, PR as %VpreMRI–MRId14 ≤ −65.0%, SD as %VpreMRI–MRId14 > −65% and < + 40%, and PD as (%VpreMRI–MRId14 ≥ + 40%).[8]

Isolation of T cells for adoptive cell transfer

After euthanizing, spleens were excised and meshed through a 70 µm cell strainer to obtain a single-cell suspension. Red blood cells were lysed with ACK buffer (150 mM

NH_4Cl, 10 mM $KHCO_3$ and 100 µM Na_2EDTA). $CD8^+$ T cells were enriched using a mouse CD8a+ T Cell Isolation Kit (Miltenyi) and LS columns. Enrichment was performed with magnetic activated cell sorting (MACS) buffer consisting of 0.5% bovine serumalbumin (BSA) and 2mM Ethylenediaminetetraacetic acid (EDTA) in PBS. T cells were cultured in T cell proliferation medium (10% FBS, 1% penicilin/streptavidine, 50µM β-mercaptoethanol, 2 mM L-glutamine, 25 mM HEPES, 1mM sodium pyruvate solution and 0.1 mM non-essential amino acids in RPMI) and stimulated with 20 U/ml IL-2, 1 µl/ml CD3 and 2 µl/ml CD28 for 48 h. After 24 h, T cells were labeled with 25 µl/ml Biopal NP for 24 h.

T cells were washed with PBS prior to adoptive cell transfer (ACT) to get rid of excess NP. $3x10^6$ $CD8^+$ T cells were diluted in 3 µl sterile PBS and stereotactically injected intratumorally with 10µl Hamilton micro-syringe driven by a fine step stereotactic device using the coordinates from tumor cell inoculation. For intraventricular injections, cells were injected 0.5 mm left from the Bregma and 1.8 mm deep using the 10 µl Hamilton micro-syringe driven by a fine step stereotactic device. Intravenous injections were performed by injecting cells diluted in 100 µl PBS in the tail vein using a 30 g needle.

Isolation of tumor-infiltrating lymphocytes

Mice were cardially perfused after receiving a lethal dose of ketamine/xylazine. For Gl261 tumors, the cerebellum was removed and the tumor-bearing hemisphere was separated from the non-tumor bearing hemisphere and processed separately. After enzymatical digestion (HBSS with 50 µg/ml Liberase D for 30min at 37°), the tissue was meshed twice through a 100 µm and 70 µm cell strainer to obtain a single-cell suspension. Myelin removal was done with a 30% Percoll gradient according to the manufacturer’s instruction.

Irradiation

Mice were anesthetized intraperetoneally with Medetomidin and Midazolam in NaCl (50 µl/10g body weight) and whole brains were irradiated with a Cu filter with 2 Gy (38 seconds). The rest of the body was protected from irradiation with a lead shield. Anesthesia was antagonized with Atipamezol and Flumazenil in NaCl (50 µl/10g body weight) subcutaneously. Irradiation was performed on day 12 and 13 after tumor inocculation.

Flow cytometry

Brain tumor cell suspensions were blocked with anti-CD16/CD32 (and the fixable viability dye FVD e780. Extracellular targets were stained for 30 min at 4°C using the antibodies listed in Table 2. For intracellular cytokine staining, cells were incubated with ionomycin, PMA and 5 µg/ml Brefeldin A for 5 h at 37°C, 5% CO2 to allow for intracellular enrichment of cytokines. Intracellular antigens were fixed, permeabilized and stained using the staining buffer set. Staining of intracellular targets was performed for 45 min at 4°C. Stained cells were analyzed on FACS Aria II. LSRFortessa or on FACS Canto II. FlowJo V10.8.1 was used for data analysis.

Immunohistochemistry

For histological correlation analysis, mice were killed in deep anesthesia by intracardial perfusion with PBS. Brains and spleens were snap frozen in Tissue-Tek® O.C.T.TM. 7 µm thick sections were cut at a CM1950 cryotome (Leica). CD3/CD90.1 co-staining was performed by fixing cryoslides with ice cold acetone (-20° C) for 10 minutes. After washing slides were blocked with 0.1% tween and 4% normal goat serum in PBS for 1 h at room temperature (RT). Slides were incubated with primary anti-CD3$^+$ antibody

(Dako, 1:200 dilution in PBS with 0.1% tween and 4% normal goat serum) overnight, washed using 0.1% tween in PBS, incubated with Alexa-546nm secondary antibody (Thermo Fisher, 1:200 dilution in 0.1% tween and 4% normal goat serum) for 1 h, washed, incubated with anti-CD90.1$^+$ (Thermo Fisher, 1:100 dilution in PBS with 0.1% tween and 4% normal goat serum) for 1 h and mounted with antifade mounting medium with DAPI (VECTASHIELD). Tile scans (10x of the entire tumor-bearing hemisphere or spleen) and higher-magnification images (40x) were acquired by confocal microscopy (Zeiss LSM700).

H&E staining

Cryoslides were thawed, incubated with haematoxylin for 5 min and rinsed with H_2O. HCL Alcohol (4ml HCL (25%) +196ml 70% Ethanol) was freshly prepared and applied for 15 seconds. Cryoslides were washed under running tap water for 10 min. Eosin was applied for 30-60 seconds and slides were washed in distilled H_2O three times, followed by an ascending alcohol row of 70% EtOH, 96% EtOH and 100% EtOH. Lastly, slides were incubated in xylol for 10 min and mounted with histomount. Images were acquired using the axioscan microscope with a 20x objective.

Prussian blue staining

Cryoslides were thawed, fixed with ice cold methanol for 10 min and rinsed with PBS. Staining was performed using the Prussian Blue staining reagent pack by BioPAL (CL-01-50): Reagent A and B were mixed in equal parts for the working solution. Working solution was applied for 10-20 min. Slides were then rinsed with distilled water three times and counterstained using a 1:50 pararosaniline solution in H_2O for 3-5 min. Lastly, slides were incubated in an ascending alcohol row of 50%, 70%, 96% and 100%

EtOH, shortly incubated in xylol and mounted with Eukit. Images were acquired using the axioscan microscope with a 20x objective.

RTCA

5,000 Gl261-Ova tumor cells/well were seeded in RTCA e-plates for in DMEM supplemented with 10 % fetal bovine serum (FBS) and 100 U/ml penicillin and 100 µg/ml streptomycin (all Sigma-Aldrich) at 37°C, 5% CO_2. After 24 h, 5,000, 10,000 or 100,000 $CD8^+$ T cells were added per well. Cells were cocultured for 7 days. Tumor cell killing was analyzed using RTCA software.

LDH release assay

LDH release assay was performed using the assay by Cell Signaling. Gl261-Ova cells and OT-1 T cells were coincubated in T cell proliferaton medium in a 96 well U bottom plate overnight at 37°, 5% CO_2. 10 µl of lysis solution was added to wells containing target cell maximum release control and volume correction and incubated for 45 min at 37°, 5% CO_2. 50 µl/sample were transferred to a 96 well flat bottom plate, 50 µl substrate was added and incubated for 30 min at RT. 50 µl stop solution was added and absorbance was measured at 490 nm using the iMark microplate absorbance reader.

FACS based killing assay

100.000 Nalm6 cells/well were seeded in a 96 well plate and 100.000 human CD19 CAR T cells (unlabeled or labeled with 50 µg Fe/1x10^6 cells for 24 h) were added. 1 µl IL-7/ml and 0.5 µl IL-15/ml were added and cells were co-incubated overnight. Cells were stained with anti-CD3 and anti-CD19 as well as fixable viability stain and counted by flow cytometry using counting beads.

ICP-OES

Primary murine T cells were incubated with the NP (5µg, 25 µg, 50 µg or 100 µg/1x10^6 cells) in TCPM for 24h, centrifuged and washed with PBS. 1 ml 65% nitric acid and 200 µl hydrogen peroxide were added to each sample to ensure cell lysis. Samples were heated at 90°C for 1 h and 8.2 ml MilliQH_2O was added for a total volume of 10 ml/sample. Analysis was performed with Agilent ICP-OES 720.

Electron microscopy

Sample preparation was performed according to Dittrich et al.[89]: Primary murine T cells were incubated with the iron oxide NP for 24 h *in vitro*, T cells were pelleted by 500 g 5 min centrifugation and fixed with 2.5% EM-grade glutaraldehyde and 2% EM-grade paraformaldehyde in 0.1 M Na-cacodylate buffer (pH 7.4) at RT for 5 min. Fixative was renewed and samples were incubated in at 4°C overnight. T cells were resuspended in 2% low-melting agarose and centrifuged at 1000 g for 10 min at 37°C, followed by 1% osmium tetroxide in dH_2O for 20 min. Cells were washed in dH_2O for 1 min four times and stained with 1% uranyl acetate in dH_2O for 14 min. Afterward, cells were rinsed in dH_2O four times for 1 min each. Dehydration with an acetone series (50%, 70%, 90%, 2 x 100%) was performed for 45 s per step in the microwave. Cells were infiltrated with EPON epoxy resin 812 (hard formula) using increasing resin concentrations in 100% acetone (10%, 30%, 50%, 70%, 90%, 3 x 100% EPON in acetone). All infiltration steps were performed in the microwave for 3 min each at 24°C. Cell pellets in 100% resin were transferred into an embedding mould, incubated at room temperature overnight, and subsequently polymerized at 60°C for 2 days. Blocks were trimmed into 200 nm thick sections. Imaging was performed using a Leica UC7 conventional ultramicrotome with a diamond knife (Diatome).

Tissue clearing

Mice were perfused with PBS and 4.5% paraformaldehyde (PFA), brains were isolated and incubated in 4.5% PFA overnight and processed using iDisco[90]: Samples were dehydrated with methanol /h2o series: 20%, 40%, 60%, 80%, 100%; 1h each. They were washed further with 100% methanol for 1h and then chilled the at 4°C followed by an overnight incubation, with shaking, in 66% DCM / 33% Methanol at RT. Samples were washed twice in 100% Methanol at RT and chilled at 4°C. They were bleached in chilled fresh 5%H_2O_2 in methanol (1 volume 30% H2O2 to 5 volumes MeOH) overnight at 4°C. Rehydration was performed with a methanol/H2O series: 80%, 60%, 40%, 20%, PBS; 1h each at RT. Next samples were washed in PTx.2 RT 1h x2 at RT. For the immunolabeling, samples were incubated in permeabilization Solution, 37°C **n** 2 days (max. 2 days), blocked in Blocking Solution, 37 °, **n** 2 days (max. 2 days) and incubated with primary antibody in PTwH/5%DMSO/3% Donkey Serum, 37°, n days. They were then washed in PTwH for 4-5 times until the next day. Incubation with secondary antibody was done in PTwH/3% Donkey Serum, 37°, n days; samples were washed in PTwH for 4-5 times until the next day. Lastly, the clearing was performed by dehydration in a methanol/H 2 O series: 20%, 40%, 60%, 80%, 100%, 100%; 1hr each at RT, followed by a 3 h incubation, with shaking, in 66% DCM / 33% Methanol at RT and incubation in 100% DCM 15 minutes twice (with shaking) to wash the MeOH. Samples were then incubated in DiBenzyl Ether. Images were acquired using light sheet microscopy (Ultramicroscope II by Miltenyi).

Indium-111 uptake (γ-counter/γ-imager)

7.5×10^6 T cells were incubated in vitro with 12.5 MBq indium-111 for 15 min in PBS and washed twice. 5×10^6 of the labeled T cells were injected intravenously in Gl261-GP100 tumor bearing mice. Mice were measured in a γ-imager 10 min, 30 min, 1 h, 2 h, 4 h, 24 h and 4 d after ACT. Organs were subsequently harvested and measured using a γ-counter.

DOTATE uptake

Primary human T cells and J76 cells that were transfected with SSTR2 as well as AR42J cells were incubated with 100.000 cpm DOTATOC for 1 h in PBS at 37 °C in 15 ml falcons while being constantly shaken. AR42J cells were purchased from cell line services (CLS) and cultured in F-12K medium + 10% FBS. The inhibitor ocreotide was added in a concentration of 10^{-5} M simultaneously with DOTATOC for uptake inhibition. Samples were subsequently washed with PBS twice and measured using a γ-counter.

Statistical analysis

Statistical analysis was performed with GraphPad Prism (version 9.3.1 for Windows, GraphPad Software, La Jolla, CA, USA). Data are represented as individual values or as mean ± SD. Significance was assessed by either unpaired t-test analysis or one-way analysis of variance (ANOVA) analysis.

Abbreviations

ACT	Adoptive cell transfer
ACK	Ammonium-Chloride-Potassium
AF	Alexa Fluor
APC	Antigen-presenting cell
BBB	Blood brain barrier
BSA	Bovine serum albumin
CAR	Chimeric antigen receptor
CEST	Chemical exchange saturation transfer
CD	Cluster of differentiation
CNS	Central nervous system
cpm	Counts per minute
CT	Computed tomography
CTLA-4	cytotoxic T-lymphocyte-associated protein 4
CR	Complete response
Cu	Copper
DAPI	4',6-Diamidino-2-phenylindol
DICOM	Digital Imaging and Communication in Medicine
DMEM	Dulbecco's Modified Eagle Medium
DMSO	Dimethyl sulfoxide
EDTA	Ethylenediaminetetraacetic acid
EGFRvIII	Epidermal growth factor receptor variant III
EM	Electron microscopy
EPI	Echo planar imaging
FACS	Fluorescence-activated cell sorting
FBS	Fetal bovine serum
Fe	Iron
FeOx	Ferumoxytol
FITC	fluorescein-5-isothiocyanate
Ga	Gallium
GBM	Glioblastoma
Gd	Gadolinium
Gy	Gray
H&E	Haematoxylin & eosin
HLA	Human leucocyte antigen

ICB	Immune checkpoint blockade
ICP-OES	Inductively coupled plasma atomic emission spectroscopy
iDISCO	immunolabeling-enabled imaging of solvent-cleared organs
IHC	immunohistochemistry
IL	interleukin
i.v.	intravenous
LDH	Lactate dehydrogenase
Lu	Lutetium
MACS	Magnetic activated cell sorting
MGE	Multi-gradient echo
MHC	major histocompatibility complex
MPI	Magnetic particle imaging
MRE	Magnetic resonance elastography
MRI	Magnetic resonance imaging
MS	Multiple sclerosis
NaCl	Sodium chloride
NP	nanoparticle
PBS	Phosphate-buffered saline
PD	Progressive disease
PD-1	Programmed cell death protein 1
PerCP	Peridinin-Chlorophyll-Protein Complex
PET	Positron emission tomography
PFA	paraformaldehyde
Pg	Picogramm
PMA	phorbol myristate acetate
PR	Partial response
RANO	Response assessment for neuro-oncology
RPMI	Roswell Park Memorial Institute Medium
RT	Room temperature
RTCA	Real-time cell assay
SD	Stable disease
SILV	silver locus protein homolog
S/MAR	Scaffold/matrix attachment region
SNIPR	SyNthetic Intramembrane Proteolysis Receptor
SOPF	Specific and Opportunistic Pathogen Free
SPIO	Superparamagnetic iron oxide

SSTR2	Somatostatin receptor 2
T	Tesla
TAM	Tumor-associated macrophages
TCR	T cell receptor
TCPM	T cell proliferation medium
TE	Echo time
TEM	Transmission electron microscopy
TME	Tumor microenvironment
TNFα	Tumor necrosis factor alpha
TR	Repetition time
Treg	T regulatory cells
USPIO	Ultrasmall superaparamagnetic iron oxide

References

1. Neth, B. J., Carabenciov, I. D., Ruff, M. W. & Johnson, D. R. Temporal Trends in Glioblastoma Survival: Progress then Plateau. *The neurologist* **27,** 119–124; 10.1097/NRL.0000000000000393 (2022).

2. Delgado-López, P. D. & Corrales-García, E. M. Survival in glioblastoma: a review on the impact of treatment modalities. *Clinical & translational oncology : official publication of the Federation of Spanish Oncology Societies and of the National Cancer Institute of Mexico* **18,** 1062–1071; 10.1007/s12094-016-1497-x (2016).

3. van Solinge, T. S., Nieland, L., Chiocca, E. A. & Broekman, M. L. D. Advances in local therapy for glioblastoma — taking the fight to the tumour. *Nat Rev Neurol* **18,** 221–236; 10.1038/s41582-022-00621-0 (2022).

4. WORLD HEALTH ORGANIZATION. *CENTRAL NERVOUS SYSTEM TUMOURS* (WORLD HEALTH ORGANIZATION, [S.l.], 2022).

5. Bunse, L., Bunse, T., Krämer, C., Chih, Y. C. & Platten, M. Clinical and Translational Advances in Glioma Immunotherapy. *Neurotherapeutics : the journal of the American Society for Experimental NeuroTherapeutics* **19**; 10.1007/s13311-022-01313-9 (2022).

6. Brahmer, J. *et al.* Nivolumab versus Docetaxel in Advanced Squamous-Cell Non-Small-Cell Lung Cancer. *The New England journal of medicine* **373,** 123–135; 10.1056/NEJMoa1504627 (2015).

7. Robert, C. *et al.* Ipilimumab plus dacarbazine for previously untreated metastatic melanoma. *The New England journal of medicine* **364,** 2517–2526; 10.1056/NEJMoa1104621 (2011).

8. Aslan, K. *et al.* Heterogeneity of response to immune checkpoint blockade in hypermutated experimental gliomas. *Nature communications* **11,** 931; 10.1038/s41467-020-14642-0 (2020).

9. Ding, R. *et al.* Single-cell transcriptome analysis of the heterogeneous effects of differential expression of tumor PD-L1 on responding TCR-T cells. *Theranostics* **11,** 4957–4974; 10.7150/thno.55075 (2021).

10. Reardon, D. A. *et al.* Effect of Nivolumab vs Bevacizumab in Patients With Recurrent Glioblastoma: The CheckMate 143 Phase 3 Randomized Clinical Trial. *JAMA oncology* **6,** 1003–1010; 10.1001/jamaoncol.2020.1024 (2020).

11. Weller, M. *et al.* Rindopepimut with temozolomide for patients with newly diagnosed, EGFRvIII-expressing glioblastoma (ACT IV): a randomised, double-blind, international phase 3 trial. *The Lancet. Oncology* **18,** 1373–1385; 10.1016/S1470-2045(17)30517-X (2017).

12. McFaline-Figueroa, J. R. & Wen, P. Y. Negative trials over and over again: How can we do better? *Neuro-oncology* **25,** 1–3; 10.1093/neuonc/noac226 (2023).

13. Ravi, V. M. *et al.* T-cell dysfunction in the glioblastoma microenvironment is mediated by myeloid cells releasing interleukin-10. *Nature communications* **13,** 925; 10.1038/s41467-022-28523-1 (2022).

14. Woroniecka, K. *et al.* T-Cell Exhaustion Signatures Vary with Tumor Type and Are Severe in Glioblastoma. *Clinical cancer research : an official journal of the American Association for Cancer Research* **24,** 4175–4186; 10.1158/1078-0432.CCR-17-1846 (2018).

15. Yin, W. *et al.* A map of the spatial distribution and tumour-associated macrophage states in glioblastoma and grade 4 IDH-mutant astrocytoma. *The Journal of pathology* **258,** 121–135; 10.1002/path.5984 (2022).

16. Engelhardt, B. Molecular mechanisms involved in T cell migration across the blood-brain barrier. *Journal of neural transmission (Vienna, Austria : 1996)* **113**; 10.1007/s00702-005-0409-y (2006).

17. Britta Engelhardt. T cell migration into the central nervous system during health and disease: Different molecular keys allow access to different central nervous system compartments. *Clinical and Experimental Neuroimmunology* **1,** 79–93; 10.1111/j.1759-1961.2010.009.x (2010).

18. Marie Bettonville *et al.* Long-term antigen exposure irreversibly modifies metabolic requirements for T cell function. *eLife* **7**; 10.7554/eLife.30938 (2018).

19. Baitsch, L. *et al.* Exhaustion of tumor-specific $CD8^+$ T cells in metastases from melanoma patients. *The Journal of clinical investigation* **121**; 10.1172/JCI46102 (2011).

20. Christine M. Bucks, Jillian A. Norton, Alina C. Boesteanu, Yvonne M. Mueller & Peter D. Katsikis. Chronic Antigen Stimulation Alone Is Sufficient to Drive CD8+ T Cell Exhaustion. *Journal of immunology (Baltimore, Md. : 1950)* **182,** 6697; 10.4049/jimmunol.0800997 (2009).

21. Kondo, T. Glioblastoma-initiating cell heterogeneity generated by the cell-of-origin, genetic/epigenetic mutation and microenvironment. *Seminars in cancer biology* **82,** 176–183; 10.1016/j.semcancer.2020.12.003 (2022).

22. Marofi, F. *et al.* CAR T cells in solid tumors: challenges and opportunities. *Stem cell research & therapy* **12,** 81; 10.1186/s13287-020-02128-1 (2021).

23. Harris, D. T. & Kranz, D. M. Adoptive T Cell Therapies: A Comparison of T Cell Receptors and Chimeric Antigen Receptors. *Trends in pharmacological sciences* **37**; 10.1016/j.tips.2015.11.004 (2016).

24. Harris, D. T. *et al.* Comparison of T Cell Activities Mediated by Human TCRs and CARs That Use the Same Recognition Domains. *Journal of immunology (Baltimore, Md. : 1950)* **200**; 10.4049/jimmunol.1700236 (2018).

25. Park, J. H. *et al.* Long-Term Follow-up of CD19 CAR Therapy in Acute Lymphoblastic Leukemia. *The New England journal of medicine* **378,** 449–459; 10.1056/NEJMoa1709919 (2018).

26. Brown, C. E. *et al.* Regression of Glioblastoma after Chimeric Antigen Receptor T-Cell Therapy. *The New England journal of medicine* **375,** 2561–2569; 10.1056/NEJMoa1610497 (2016).

27. Brown, C. E. *et al.* Off-the-shelf, steroid-resistant, IL13Rα2-specific CAR T cells for treatment of glioblastoma. *Neuro-oncology* **24**; 10.1093/neuonc/noac024 (2022).

28. Majzner, R. G. *et al.* GD2-CAR T cell therapy for H3K27M-mutated diffuse midline gliomas. *Nature* **603,** 934–941; 10.1038/s41586-022-04489-4 (2022).

29. Salinas, R. D., Durgin, J. S. & O'Rourke, D. M. Potential of Glioblastoma-Targeted Chimeric Antigen Receptor (CAR) T-Cell Therapy. *CNS drugs* **34,** 127–145; 10.1007/s40263-019-00687-3 (2020).

30. Bagley, S. J., Desai, A. S., Linette, G. P., June, C. H. & O'Rourke, D. M. CAR T-cell therapy for glioblastoma: recent clinical advances and future challenges. *Neuro-oncology* **20,** 1429–1438; 10.1093/neuonc/noy032 (2018).

31. Gao, J., Liang, Y. & Wang, L. Shaping Polarization Of Tumor-Associated Macrophages In Cancer Immunotherapy. *Frontiers in immunology* **13,** 888713; 10.3389/fimmu.2022.888713 (2022).

32. Klug, F. *et al.* Low-dose irradiation programs macrophage differentiation to an iNOS$^+$/M1 phenotype that orchestrates effective T cell immunotherapy. *Cancer cell* **24,** 589–602; 10.1016/j.ccr.2013.09.014 (2013).

33. Kersten, K. *et al.* Spatiotemporal co-dependency between macrophages and exhausted CD8+ T cells in cancer. *Cancer cell* **40,** 624-638.e9; 10.1016/j.ccell.2022.05.004 (2022).

34. Natalia Ochocka *et al.* Single-cell RNA sequencing reveals functional heterogeneity of glioma-associated brain macrophages. *Nature communications* **12**; 10.1038/s41467-021-21407-w (2021).

35. Rodell, C. B. *et al.* TLR7/8-agonist-loaded nanoparticles promote the polarization of tumour-associated macrophages to enhance cancer immunotherapy. *Nature biomedical engineering* **2,** 578–588; 10.1038/s41551-018-0236-8 (2018).

36. Turco, V. *et al.* T cell-independent eradication of experimental glioma by intravenous TLR7/8-agonist-loaded nanoparticles. *Nature communications* **14,** 771; 10.1038/s41467-023-36321-6 (2023).

37. Xu, L. *et al.* Reshaping the systemic tumor immune environment (STIE) and tumor immune microenvironment (TIME) to enhance immunotherapy efficacy in solid tumors. *J Hematol Oncol* **15,** 1–30; 10.1186/s13045-022-01307-2 (2022).

38. Ma, Y., Wang, Q., Dong, Q., Zhan, L. & Zhang, J. How to differentiate pseudoprogression from true progression in cancer patients treated with immunotherapy. *American Journal of Cancer Research* **9,** 1546–1553 (2019).

39. Foray, C. *et al.* Imaging temozolomide-induced changes in the myeloid glioma microenvironment. *Theranostics* **11,** 2020–2033; 10.7150/thno.47269 (2021).

40. Hygino da Cruz, L. C., Rodriguez, I., Domingues, R. C., Gasparetto, E. L. & Sorensen, A. G. Pseudoprogression and pseudoresponse: imaging challenges in the assessment of posttreatment glioma. *AJNR. American journal of neuroradiology* **32,** 1978–1985; 10.3174/ajnr.A2397 (2011).

41. Okada, H. *et al.* Immunotherapy response assessment in neuro-oncology: a report of the RANO working group. *The Lancet. Oncology* **16,** e534-e542; 10.1016/S1470-2045(15)00088-1 (2015).

42. Weishaupt, D., Köchli, V. D. & Marincek, B. *Wie funktioniert MRI? Eine Einführung in Physik und Funktionsweise der Magnetresonanzbildgebung.* 7th ed. (Springer, Berlin, 2014).

43. Thu, M. S. *et al.* Self-Assembling Nanocomplexes by combining Ferumoxytol, Heparin And Protamine For Cell Tracking by MRI. *Nature medicine* **18,** 463–467; 10.1038/nm.2666 (2012).

44. Kiru, L. *et al.* In vivo imaging of nanoparticle-labeled CAR T cells. *Proceedings of the National Academy of Sciences of the United States of America* **119**; 10.1073/pnas.2102363119 (2022).

45. Szatmári, T. *et al.* Detailed characterization of the mouse glioma 261 tumor model for experimental glioblastoma therapy. *Cancer science* **97**; 10.1111/j.1349-7006.2006.00208.x (2006).

46. Galldiks, N. *et al.* Investigational PET tracers in neuro-oncology—What's on the horizon? A report of the PET/RANO group. *Neuro Oncol* **24,** 1815–1826; 10.1093/neuonc/noac131 (2022).

47. Vedvyas, Y. *et al.* Longitudinal PET imaging demonstrates biphasic CAR T cell responses in survivors. *JCI insight* **1,** e90064; 10.1172/jci.insight.90064 (2016).

48. Argyros, O. *et al.* Persistent episomal transgene expression in liver following delivery of a scaffold/matrix attachment region containing non-viral vector. *Gene Ther* **15,** 1593–1605; 10.1038/gt.2008.113 (2008).

49. Theveniau, M. A., Yasuda, K., Bell, G. I. & Reisine, T. Immunological detection of isoforms of the somatostatin receptor subtype, SSTR2. *Journal of neurochemistry* **63,** 447–455; 10.1046/j.1471-4159.1994.63020447.x (1994).

50. Kim, S. J. *et al.* Superparamagnetic iron oxide nanoparticles for direct labeling of stem cells and in vivo MRI tracking. *Contrast media & molecular imaging* **11,** 55–64; 10.1002/cmmi.1658 (2016).

51. Bull, E. *et al.* Stem cell tracking using iron oxide nanoparticles. *International Journal of Nanomedicine* **9,** 1641–1653; 10.2147/IJN.S48979 (2014).

52. Li, L. *et al.* Superparamagnetic Iron Oxide Nanoparticles as MRI contrast agents for Non-invasive Stem Cell Labeling and Tracking. *Theranostics* **3,** 595–615; 10.7150/thno.5366 (2013).

53. Charpentier, J. C. *et al.* Macropinocytosis drives T cell growth by sustaining the activation of mTORC1. *Nat Commun* **11,** 1–9; 10.1038/s41467-019-13997-3 (2020).

54. Means, N., Elechalawar, C. K., Chen, W. R., Bhattacharya, R. & Mukherjee, P. Revealing macropinocytosis using nanoparticles. *Molecular Aspects of Medicine* **83,** 100993; 10.1016/j.mam.2021.100993 (2022).

55. Rivera-Rodriguez, A. *et al.* Tracking adoptive T cell immunotherapy using magnetic particle imaging. *Nanotheranostics* **5,** 431–444; 10.7150/ntno.55165 (2021).

56. Liu, H. *et al.* Biocompatible Iron Oxide Nanoring-Labeled Mesenchymal Stem Cells: An Innovative Magnetothermal Approach for Cell Tracking and Targeted Stroke Therapy. *ACS nano* **16,** 18806–18821; 10.1021/acsnano.2c07581 (2022).

57. Masthoff, M. *et al.* Resolving immune cells with patrolling behaviour by magnetic resonance time-lapse single cell tracking. *EBioMedicine* **73,** 103670; 10.1016/j.ebiom.2021.103670 (2021).

58. Agliardi, G. *et al.* Intratumoral IL-12 delivery empowers CAR-T cell immunotherapy in a pre-clinical model of glioblastoma. *Nat Commun* **12,** 1–11; 10.1038/s41467-020-20599-x (2021).

59. Jing, Y. *et al.* Expression of chimeric antigen receptor therapy targets detected by single-cell sequencing of normal cells may contribute to off-tumor toxicity. *Cancer cell* **39,** 1558–1559; 10.1016/j.ccell.2021.09.016 (2021).

60. Schaettler, M. O. *et al.* TCR-engineered adoptive cell therapy effectively treats intracranial murine glioblastoma. *Journal for immunotherapy of cancer* **11**; 10.1136/jitc-2022-006121 (2023).

61. McConnell, H. L. *et al.* Ferumoxytol nanoparticle uptake in brain during acute neuroinflammation is cell-specific. *Nanomedicine : nanotechnology, biology, and medicine* **12,** 1535–1542; 10.1016/j.nano.2016.03.009 (2016).

62. Vazquez-Lombardi, R. *et al.* High-throughput T cell receptor engineering by functional screening identifies candidates with enhanced potency and specificity. *Immunity* **55**; 10.1016/j.immuni.2022.09.004 (2022).

63. Chen, D. *et al. A microglia-CD4 + T cell partnership generates protective anti-tumor immunity to glioblastoma* (2022).

64. Cohen, M. *et al.* The interaction of CD4+ helper T cells with dendritic cells shapes the tumor microenvironment and immune checkpoint blockade response. *Nature cancer* **3,** 303–317; 10.1038/s43018-022-00338-5 (2022).

65. Friedrich, M. *et al.* Dysfunctional dendritic cells limit antigen-specific T cell response in glioma. *Neuro-oncology*; 10.1093/neuonc/noac138 (2022).

66. Sagiv-Barfi, I., Czerwinski, D. K., Shree, T., Lohmeyer, J. J. K. & Levy, R. Intratumoral immunotherapy relies on B and T cell collaboration. *Science immunology* **7,** eabn5859; 10.1126/sciimmunol.abn5859 (2022).

67. Liu, S., Liu, X., Zhang, C., Shan, W. & Qiu, X. T-Cell Exhaustion Status Under High and Low Levels of Hypoxia-Inducible Factor 1α Expression in Glioma. *Front. Pharmacol.* **12**; 10.3389/fphar.2021.711772 (2021).

68. Boieri, M. *et al.* CD4+ T helper 2 cells suppress breast cancer by inducing terminal differentiation. *The Journal of experimental medicine* **219**; 10.1084/jem.20201963 (2022).

69. Alspach, E. *et al.* MHC-II neoantigens shape tumour immunity and response to immunotherapy. *Nature* **574,** 696–701; 10.1038/s41586-019-1671-8 (2019).

70. Loai, Y., Ganesh, T. & Cheng, H.-L. M. Concurrent dual contrast for cellular magnetic resonance imaging using gadolinium oxide and iron oxide nanoparticles. *International journal of molecular imaging* **2012,** 230942; 10.1155/2012/230942 (2012).

71. Gordon, S. Phagocytosis: An Immunobiologic Process. *Immunity* **44,** 463–475; 10.1016/j.immuni.2016.02.026 (2016).

72. Ng, T. S. C. *et al.* Detecting Immune Response to Therapies Targeting PDL1 and BRAF by Using Ferumoxytol MRI and Macrin in Anaplastic Thyroid Cancer. *Radiology* **298,** 123–132; 10.1148/radiol.2020201791 (2021).

73. Mohanty, S. *et al.* Nanoparticle enhanced MRI can monitor macrophage response to CD47 mAb immunotherapy in osteosarcoma. *Cell death & disease* **10,** 36; 10.1038/s41419-018-1285-3 (2019).

74. Liu, M. *et al.* Metabolic rewiring of macrophages by CpG potentiates clearance of cancer cells and overcomes tumor-expressed CD47-mediated 'don't-eat-me' signal. *Nature immunology* **20,** 265–275; 10.1038/s41590-018-0292-y (2019).

75. Meir, R. *et al.* Nanomedicine for Cancer Immunotherapy: Tracking Cancer-Specific T-Cells in Vivo with Gold Nanoparticles and CT Imaging. *ACS nano* **9,** 6363–6372; 10.1021/acsnano.5b01939 (2015).

76. Nagle, V. L. *et al.* Imaging Tumor-Infiltrating Lymphocytes in Brain Tumors with 64CuCu-NOTA-anti-CD8 PET. *Clinical cancer research : an official journal of the American Association for Cancer Research* **27,** 1958–1966; 10.1158/1078-0432.CCR-20-3243 (2021).

77. Nagle, V. L. *et al.* Noninvasive Imaging of CD4+ T Cells in Humanized Mice. *Molecular cancer therapeutics* **21,** 658–666; 10.1158/1535-7163.MCT-21-0888 (2022).

78. Woodham, A. W. *et al.* In vivo detection of antigen-specific CD8+ T cells by immuno-positron emission tomography. *Nature methods* **17,** 1025–1032; 10.1038/s41592-020-0934-5 (2020).

79. Shin, J. *et al.* Antigen-dependent inducible T cell reporter system for PET imaging of breast cancer and glioblastoma. *Journal of nuclear medicine : official publication, Society of Nuclear Medicine*; 10.2967/jnumed.122.264284 (2022).

80. Farrell, B. T. *et al.* Using iron oxide nanoparticles to diagnose CNS inflammatory diseases and PCNSL. *Neurology* **81,** 256–263; 10.1212/WNL.0b013e31829bfd8f (2013).

81. Hamilton, B. E. *et al.* Comparative analysis of ferumoxytol and gadoteridol enhancement using T1- and T2-weighted MRI in neuroimaging. *AJR. American journal of roentgenology* **197,** 981–988; 10.2214/AJR.10.5992 (2011).

82. Anne M. Muehe *et al.* Safety Report of Ferumoxytol for Magnetic Resonance Imaging in Children and Young Adults. *Investigative radiology* **51,** 221; 10.1097/RLI.0000000000000230 (2016).

83. Zhang, H., Zhou, J. & Peng, Y. Amide Proton Transfer-Weighted MR Imaging of Pediatric Central Nervous System Diseases. *Magnetic resonance imaging clinics of North America* **29,** 631–641; 10.1016/j.mric.2021.06.012 (2021).

84. Sui, R. *et al.* Whole-brain amide CEST imaging at 3T with a steady-state radial MRI acquisition. *Magnetic resonance in medicine* **86,** 893–906; 10.1002/mrm.28770 (2021).

85. Chauvet, D. *et al.* In-vivo-Messung der Elastizität von Hirntumoren mittels intraoperativer Scherwellen-Elastografie. *Ultraschall in der Medizin (Stuttgart, Germany : 1980)* **37,** 584–590; 10.1055/s-0034-1399152 (2016).

86. Jiang, Y. *et al.* Noninvasive imaging evaluation of tumor immune microenvironment to predict outcomes in gastric cancer. *Annals of oncology : official journal of the European Society for Medical Oncology* **31,** 760–768; 10.1016/j.annonc.2020.03.295 (2020).

87. Silva, R. V. *et al.* Contribution of Tissue Inflammation and Blood-Brain Barrier Disruption to Brain Softening in a Mouse Model of Multiple Sclerosis. *Frontiers in neuroscience* **15,** 701308; 10.3389/fnins.2021.701308 (2021).

88. Gate, D. *et al.* CD4+ T cells contribute to neurodegeneration in Lewy body dementia. *Science (New York, N.Y.)* **374,** 868–874; 10.1126/science.abf7266 (2021).

89. Dittrich, T. *et al.* A high-throughput electron tomography workflow reveals over-elongated centrioles in relapsed/refractory multiple myeloma. *Cell Reports Methods* **2,** 100322; 10.1016/j.crmeth.2022.100322 (2022).

90. Renier, N. *et al.* iDISCO: a simple, rapid method to immunolabel large tissue samples for volume imaging. *Cell* **159**; 10.1016/j.cell.2014.10.010 (2014).